

Remote Sensing of Cloud, Aerosol, and Water Vapor Properties from the Moderate Resolution Imaging Spectrometer (MODIS)

Michael D. King, Yoram J. Kaufman, W. Paul Menzel, and Didier Tanré

Abstract—The Moderate Resolution Imaging Spectrometer (MODIS) is an earth-viewing sensor being developed as a facility instrument for the Earth Observing System (EOS) to be launched in the late 1990's. MODIS consists of two separate instruments that scan a swath width sufficient to provide nearly complete global coverage every 2 days from a polar-orbiting, sun-synchronous, platform at an altitude of 705 km. MODIS-N (nadir) will provide images in 36 spectral bands between 0.415 and 14.235 μm with spatial resolutions of 250 m (2 bands), 500 m (5 bands), and 1000 m (29 bands). These bands have been carefully selected to enable advanced studies of land, ocean, and atmospheric processes. In this paper we describe the status of MODIS-N and its companion instrument MODIS-T (tilt), a tiltable cross-track scanning spectrometer with 32 uniformly spaced channels between 0.410 and 0.875 μm . In addition, we review the various methods being developed for the remote sensing of atmospheric properties using MODIS, placing primary emphasis on the principal atmospheric applications of determining the optical, microphysical, and physical properties of clouds and aerosol particles from spectral reflection and thermal emission measurements. In addition to cloud and aerosol properties, MODIS-N will be used for determining the total precipitable water vapor and atmospheric stability. The physical principles behind the determination of each of these atmospheric products will be described herein, together with an example of their application to aircraft and/or satellite measurements. Extensions of these and related methods to MODIS observations pose an extraordinary challenge as well as a unique opportunity to enhance our understanding of the earth-atmosphere-ocean system.

I. INTRODUCTION

The Moderate Resolution Imaging Spectrometer (MODIS) being developed for the Earth Observing System (EOS) is well suited to the global monitoring of atmospheric properties from space. In addition to the inherent interest in the atmospheric properties to be determined from this sensor system, MODIS will enable multidisciplinary studies of earth-atmosphere and ocean-atmosphere interactions to be explored. The wide spectral range of the MODIS-N channels (0.42–14.24 μm), together with the combination of frequent global coverage (1–2 days revisit) and two high spatial res-

olution channels (250 m), will permit state-of-the-art global monitoring of atmospheric water vapor, aerosol particles, and the subsequently formed clouds. Data collected by MODIS will provide information about the climatology and dynamics of atmospheric properties, the impact of human activity on the regional and global environment, and the interaction and subsequent impact of man on terrestrial and oceanic biota. This information will undoubtedly be instrumental in helping to make key scientific and political decisions that will face us in the next two decades regarding the use and misuse of the natural environment.

Among the atmospheric properties to be examined using MODIS observations, clouds are especially important, since they are a strong modulator of the shortwave and longwave components of the earth's radiation budget [68], [70]. The importance of clouds and radiation in studies of the earth's climate has recently been demonstrated both from observations [69] and from modeling [10] studies. Current data sets have revealed intriguing relationships between clouds, the earth's radiation budget and climate. EOS will provide an unprecedented opportunity to examine these relationships using a combination of simultaneous MODIS-N cloud observations and CERES (Clouds and the Earth's Radiant Energy System) measurements of broadband radiation [6].

A knowledge of cloud properties and their variation in space and time is especially crucial to studies of global climate change (e.g., trace gas greenhouse effects), as general circulation model (GCM) simulations indicate climate-induced changes in cloud amount and vertical structure, with a corresponding feedback working to enhance global warming [99]. GCM simulations by Roeckner *et al.* [75] and Mitchell *et al.* [57], which included corresponding changes in liquid water content and cloud optical thickness, further suggest that changes in cloud optical properties may result in a negative feedback comparable in size to the positive feedback associated with changes in cloud cover. None of the GCM simulations to date include corresponding changes in cloud microphysical properties (e.g., particle size), which could easily modify conclusions obtained thus far. Thus the remote sensing of the optical, microphysical, and physical properties of clouds from spectral reflection and emission measurements is exceedingly important for an improved understanding of the earth's climate system.

Clouds occur in the earth's atmosphere as a result of the widespread distribution of aerosol particles that serve as the

Manuscript submitted December 14, 1990; revised July 17, 1991.

M. D. King and Y. J. Kaufman are with the Laboratory for Atmospheres, NASA Goddard Space Flight Center, Greenbelt, MD 20771.

W. P. Menzel is with the Advanced Satellite Products Project, NOAA/NESDIS, Madison, WI 53706.

Didier Tanré is with the Laboratoire d'Optique Atmosphérique, Université des Sciences et Technique de Lille, Villeneuve d'Ascq, France.

IEEE Log Number 9103327.

primary source of cloud condensation nuclei (CCN). The effect of both natural and anthropogenic aerosols on cloud physics, chemistry, and albedo is an active area of research [92], [38]. Charlson *et al.* [13] argue that the major source of CCN in the marine environment is dimethylsulfide (DMS) produced by phytoplankton. Furthermore, the possibility exists that the expected increase in anthropogenic aerosol can result in clouds with higher albedos, as Coakley *et al.* [16] and Radke *et al.* [66] have demonstrated from satellite and *in situ* aircraft observations of clouds modified by ship track effluents. Twomey *et al.* [94] analyzed the effects of anthropogenic aerosols on cloud albedo and concluded that the loss of sunlight may compensate for the expected warming by CO₂. Kaufman *et al.* [44] compared the radiative forcing due to the emission of SO₂ from the burning of fossil fuels and concluded that it is presently more likely that fossil fuel burning causes cooling of the atmosphere due to the effect of SO₂-induced aerosols on clouds. Wigley [103] further raised the possibility that the large increase in SO₂ emissions that has occurred in the northern hemisphere this century may have resulted in greater sulfate CCN and, therefore, enhanced cooling of the northern hemisphere, relative to the southern hemisphere. Thus the simultaneous study and global observations of both cloud and aerosol optical properties is of paramount importance to the enhanced understanding of the global climate system [32].

In addition to their interaction with clouds, aerosol particles are important components of the earth-atmosphere system, affecting atmospheric visibility, the earth's radiation budget, and the remote sensing of the earth's surface from space [24], [26]. In fact, due to their effect on solar radiation (directly and through their effect on clouds), aerosol particles are considered in a recent review article by Hansen and Lacis [32] to be "the source of our greatest uncertainty about climate forcing." Wind-blown dust from desert regions, anthropogenic emissions from industrial activity, sea salt aerosol from bursting bubbles at the ocean surface, and biomass burning in the tropical rain forests are all important sources of atmospheric aerosol particles. Saharan dust, for example, is often transported across the Atlantic and deposited in the southeastern U. S. [8] or carried across the Mediterranean to Europe [81]. Sedimentation of desert dust is an important source of minerals both for land and oceanic regions [65]. Anthropogenic emission of SO₂ [36], which contributes significantly to the acidity of precipitation, is also responsible for the generation of sulfate aerosol particles and, hence, CCN. Remote sensing of aerosol properties from space [30], [27], [43], [22] can thus reveal the sources, transport pathways, and sinks of these particulates, which, in turn, can be used as a tracer of the emission of the gaseous precursors of these particulates, which themselves affect the environment (e. g., [7]). Organic particulates are also emitted along with greenhouse trace gases and NO_x in the process of biomass burning [96], [45]. Therefore, these particles can be used as a tracer for gases emitted from biomass burning, for monitoring their sources and transport, and to assess their impact on atmospheric chemistry, acid deposition, and climate.

Remote sensing of the total precipitable water vapor is also important for an increased understanding of the global hydrologic cycle, biosphere-atmosphere interactions, the earth's radiant energy budget, and for monitoring climate change processes associated with changes in greenhouse gases. For example, water vapor itself is a greenhouse gas, thereby leading to a positive feedback when the climate warms due to increased emissions of CO₂, thereby accelerating the warming trend due to the initial forcing that arises from the burning of fossil fuels [72], [9]. It is particularly important to monitor seasonal and annual changes in the precipitable water on regional scales in order to monitor drought conditions and desertification processes. The sparse location of ground monitoring stations, mainly located in dry areas, calls for an accurate remote sensing technique that can provide water vapor information on a daily basis with a spatial resolution of 1–5 km.

The intent of this paper is to describe the current status of the MODIS facility being developed for EOS, and to review the physical principles behind the remote sensing of atmospheric properties using this sensor system. Since the development of the science and algorithms to reduce MODIS data is at its earliest stages, this review is based primarily on generic methods and methods previously developed for processing data from other sensors with similar spectral characteristics. Through the activity of the MODIS science team we anticipate that these methods will be adapted for use in the processing of MODIS data, both through simulations and through airborne field experiments. After a brief description of the MODIS-N and MODIS-T instruments, we will outline the concepts being developed for the determination of the optical, microphysical, and physical properties of clouds and aerosol particles, as well as methods for determining the total precipitable water vapor and atmospheric stability from spectral reflection and thermal emission measurements to be obtained from space.

II. MODIS-N

MODIS-N (nadir) is a 36-channel scanning radiometer whose band center and bandwidth characteristics are summarized in Table I. This instrument is designed to scan through nadir in a plane perpendicular to the velocity vector of the spacecraft, with the maximum scan extending up to 55° on either side of nadir (110° aperture). At a nominal orbital altitude for the EOS platform of 705 km, this yields a swath width of 2330 km centered on the satellite ground track. In the baseline concept, the earth-emitted and reflected solar radiation is incident on a two-sided scan mirror that continually rotates about an axis aligned with the direction of flight. Following the scan mirror is a telescope and a sequence of three dichroic beam splitters that further subdivide the incoming radiation into four focal planes. Each spectral band uses a ten-element linear array detector for the 1000-m spatial resolution bands (channels 8–36), a 20-element array for the 500-m bands (channels 3–7) and a 40-element array for the 250-m bands (channels 1 and 2), and are aligned parallel to one another such that a single scan of the scan mirror is imaged on the focal plane for a swath 10 km in the along-

TABLE I
SPECTRAL CHARACTERISTICS, SPATIAL RESOLUTION, SATURATION REFLECTION FUNCTION (AT $\theta_0 = 22.5^\circ$),
SATURATION BRIGHTNESS TEMPERATURE AND PRINCIPAL PURPOSES OF ALL ATMOSPHERIC CHANNELS OF MODIS-N

Channel	λ (μm)	$\Delta\lambda$ (μm)	Ground resolution (m)	R_{max}	$T_{\text{max}}(\text{K})$	Atmospheric Purpose
1	0.659	0.050	250	1.49		Aerosol Properties and Cloud Optical Thickness
2	0.865	0.040	250	1.00		Aerosol Properties
3	0.470	0.020	500	1.04		Aerosol Mass Loading and Optical Thickness
4	0.555	0.020	500	0.93		Aerosol Optical Thickness
5	1.240	0.020	500	0.51		Aerosol Optical Thickness
6	1.640	0.020	500	1.02		Snow/Cloud Discrimination; Cloud Phase; Aerosol Optical Thickness
7	2.130	0.050	500	0.81		Cloud Effective Particle Radius; Aerosol Optical Thickness
8	0.415	0.015	1000	0.33		Aerosol Optical Thickness
9	0.443	0.010	1000	0.23		
10	0.490	0.010	1000	0.17		
11	0.531	0.010	1000	0.15		
12	0.565	0.010	1000	0.12		
13	0.653	0.015	1000	0.08		
14	0.681	0.010	1000	0.07		
15	0.750	0.010	1000	0.07		
16	0.865	0.015	1000	0.06		
17	0.905	0.030	1000	0.67		Total Precipitable Water
18	0.936	0.010	1000	1.00		Total Precipitable Water and Cloud Fraction
19	0.940	0.050	1000	0.74		Total Precipitable Water and Cloud Fraction
20	3.750	0.180	1000		335	Cloud Effective Particle Radius; Cloud and Surface Temperature
21	3.750	0.050	1000		700	Fire and Volcano Temperature
22	3.959	0.050	1000		328	Cloud and Surface Temperature
23	4.050	0.050	1000		328	Cloud and Surface Temperature
24	4.465	0.050	1000		264	Temperature Profile
25	4.515	0.050	1000		285	Temperature Profile
26	4.565	0.050	1000		302	Temperature Profile
27	6.715	0.360	1000		271	Mid-Tropospheric Water Vapor
28	7.325	0.300	1000		275	Upper-Tropospheric Water Vapor
29	8.550	0.300	1000		324	Surface Temperature; Cloud Effective Particle Radius; Cirrus Detection
30	9.730	0.300	1000		275	Total Ozone Content
31	11.030	0.300	1000		400	Cloud and Surface Temperature; Fire and Volcano Temperature
32	12.020	0.500	1000		400	Cloud and Surface Temperature; Fire and Volcano Temperature
33	13.335	0.300	1000		285	Cloud Top Pressure and Temperature; Temperature Profile
34	13.635	0.300	1000		268	Cloud Top Pressure and Temperature; Temperature Profile
35	13.935	0.300	1000		261	Cloud Top Pressure and Temperature; Temperature Profile
36	14.235	0.300	1000		238	Cloud Top Pressure and Temperature; Temperature Profile

track direction and 2330 km in the cross-track direction. In this configuration, all channels within a single focal plane ($0.42\text{--}0.57\ \mu\text{m}$, $0.65\text{--}0.94\ \mu\text{m}$, $1.24\text{--}4.57\ \mu\text{m}$, $6.72\text{--}14.24\ \mu\text{m}$) are simultaneously sampled and coregistered, with registration errors of less than 100 m between focal planes. The signal-to-noise ratio (SNR) ranges between 57 and 1100 at a solar zenith angle $\theta_0 = 70^\circ$, depending on the channel, and is considerably larger than these values at the solar zenith angle and scene temperature typical of the EOS orbit ($\theta_0 = 22.5^\circ$). Operating at 12-b digitization and a 100% duty cycle, the orbital average data rate of this instrument is expected to be 5.1 Mbps (55 Gbyte per day). Table I also summarizes the dynamic range and main purpose(s) of each MODIS-N channel to be used for atmospheric processing of global data. Additional purposes for the MODIS-N bands, together with a description of the processing scenarios currently envisioned for producing ocean, land, and atmospheric products from MODIS, can be found in Ardanuy *et al.* [3].

III. MODIS-T

MODIS-T (tilt) is an along-track pointable, cross-track scanning spectrometer with 32 spectral bands uniformly spaced between 0.410 and $0.875\ \mu\text{m}$ with bandwidths ranging between 0.011 and $0.014\ \mu\text{m}$. This instrument uses a solid-state charge coupled device (CCD) array detector of the "whiskbroom" type to scan a swath width 45° on either side of nadir (90° aperture), with each scan consisting of 30 pixels in the along-track direction. Thus from a nominal orbital altitude of 705 km, each scan of the spectrometer yields a swath width 1500 km in the cross-track direction and 33 km in the along-track direction, with each pixel having a spatial resolution of 1.1 km at nadir. One of the unique features of this spectrometer is its ability to tilt up to 67.5° fore and 50° aft, thereby permitting useful ocean optics measurements to be obtained in regions that would otherwise be adversely affected by sunglint. Furthermore, land applications such as

determining the bidirectional reflectance function of plant canopies can be pursued when not observing the ocean. As presently conceived, this instrument will operate in a dual-gain mode such that data will be acquired both at low and high gain levels simultaneously. In this way data that are saturated in the high-gain (ocean) mode will be transmitted to the ground in the low-gain (land and cloud) mode for further processing. For atmospheric applications, MODIS-T is secondary to the primary atmospheric uses of MODIS-N, to be described in the following sections. The SNR for each channel in the ocean (nonocean) mode will generally exceed 800 (280) at the shortest wavelength, decreasing (increasing) to near 300 (400) at the longest wavelength. The orbital average data rate of this instrument will be 1.2 Mbps (13 Gbyte per day).

IV. CLOUD PROPERTIES

A. Cloud Optical Thickness and Effective Particle Radius

When the optical thickness of the atmosphere is sufficiently large, numerical results for the reflection function must agree with known asymptotic expressions for very thick layers [95], where the reflection function $R(\tau_c; \mu, \mu_0, \phi)$ is formed from a ratio of the reflected intensity (radiance) $I(0, -\mu, \phi)$ and the incident solar flux F_0 , and is defined by

$$R(\tau_c; \mu, \mu_0, \phi) = \frac{\pi I(0, -\mu, \phi)}{\mu_0 F_0}. \quad (1)$$

In this expression τ_c is the total optical thickness of the atmosphere (or cloud), μ_0 the cosine of the solar zenith angle θ_0 , μ the absolute value of the cosine of the zenith angle θ , measured with respect to the positive τ direction, and ϕ the relative azimuth angle between the direction of propagation of the emerging radiation and the incident solar direction.

Numerical simulations as well as asymptotic theory show that the reflection properties of optically thick layers depend essentially on two parameters, the scaled optical thickness τ'_c and the similarity parameter s , defined by

$$\tau'_c = (1 - \omega_0 g) \tau_c \quad (2)$$

$$s = \left(\frac{1 - \omega_0}{1 - \omega_0 g} \right)^{\frac{1}{2}} \quad (3)$$

where g is the asymmetry factor and ω_0 the single scattering albedo of a small volume of the cloud layer. In addition, the reflectance properties of the earth-atmosphere system depend on the reflectance (albedo) of the underlying surface, A_g . The similarity parameter, in turn, depends primarily on the effective particle radius, defined by [34]

$$r_e = \int_0^\infty r^3 n(r) dr / \int_0^\infty r^2 n(r) dr \quad (4)$$

where $n(r)$ is the particle size distribution and r is the particle radius. In addition to τ'_c , s and A_g , the details of the single scattering phase function affect the directional reflectance of the cloud layer [47].

Fig. 1 illustrates the spherical albedo as a function of wavelength for water clouds containing various values of the effective radius. Since the spherical albedo represents

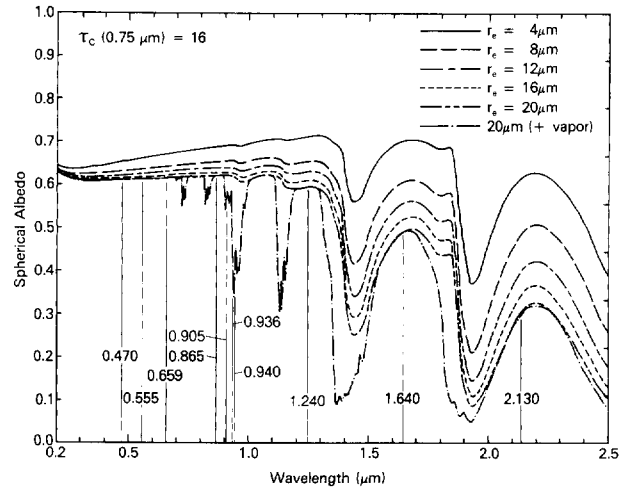


Fig. 1. Cloud spherical albedo as a function of wavelength for selected values of the effective radius of cloud droplets. Results apply to waterclouds having a modified gamma size distribution with an effective variance $v_e = 0.111$, an optical thickness $\tau_c(0.75 \mu\text{m}) = 16$, and saturated water vapor $w_g = 0.45 \text{ g cm}^{-2}$.

a mean value of the reflection function over all solar and observational zenith and azimuth angles, the reflection function itself must have a similar sensitivity to particle size. These computations were performed using asymptotic theory for thick layers and the complex refractive indices of liquid water, and include the additional contribution of water vapor. These computations strictly apply to the case when $\tau_c(0.75 \mu\text{m}) = 16$ and $A_g = 0.0$, and properly allow for the optical thickness and asymmetry factor to vary with wavelength in accord with our expectations for clouds composed solely of liquid water and water vapor (see King *et al.* [48] for details). Since the similarity parameter is nearly zero (conservative scattering) in the water vapor windows at wavelengths $\lambda \lesssim 1.0 \mu\text{m}$, the cloud optical thickness can be derived primarily from reflection function measurements in this wavelength region. Fig. 1 also shows that the spherical albedo, and hence reflection function, is sensitive to particle size at wavelengths near 1.64 and 2.13 μm , wavelengths for which water vapor absorption is small.

The principles outlined above form the basis of methods for simultaneously retrieving the cloud optical thickness and effective radius from multiwavelength reflected solar radiation measurements [17], [23], [58], [73], [93]. The interest in retrieving the optical thickness and effective radius derives not only from the fact that such a retrieval seems possible, but from the fact that shortwave plane-parallel cloud radiative properties depend almost exclusively on these two parameters. This thus forms the basis of cloud radiative parameterization methods, such as the one recently introduced by Slingo [82], which require that a global data base on the effective radius and optical thickness (or equivalently integrated liquid water content) of clouds be available. Such data seem only to be derivable from spaceborne remote sensing observations. Fig. 1 shows the wavelength locations of the visible and near-infrared channels of MODIS-N, located primarily in the water vapor window regions. MODIS-N is, therefore, ideally suited to cloud remote sensing applications.

The sensitivity of the reflection function to cloud optical thickness and effective radius can perhaps best be understood upon examination of Fig. 2, which shows simultaneous calculations of the reflection function at 0.75 and 2.16 μm for various values of τ_c and r_e when $\theta_0 = 45.7^\circ$, $\theta = 28.0^\circ$ and $\phi = 63.9^\circ$ [58]. These wavelengths were chosen because they are outside the water vapor and oxygen absorption bands and yet have substantially different water droplet (or ice particle) absorption characteristics (cf. Fig. 1). These wavelengths correspond to two channels of the Multispectral Cloud Radiometer (MCR) described by Curran *et al.* [18] and King [47], but may readily be adapted to comparable channels (0.66 and 2.13 μm) of MODIS-N (channels 1 and 7).

Fig. 2 clearly illustrates the underlying principles behind the simultaneous determination of τ_c and r_e from reflected solar radiation measurements. The minimum value of the reflection function at each wavelength corresponds to the reflection function of the underlying surface at that wavelength in the absence of an atmosphere ($\tau_c = 0$). For the computations presented in Fig. 2, the underlying surface was assumed to be Lambertian with $A_g = 0.06$, roughly corresponding to an ocean surface under diffuse illumination conditions. The dashed curves represent the reflection functions at 0.75 and 2.16 μm that result for specified values of the cloud optical thickness, while the solid curves represent the reflection functions that result for specified values of the effective radius. These results show, for example, that the cloud optical thickness is largely determined by the reflection function at a nonabsorbing wavelength (0.75 μm in this case), with little dependence on droplet radius. The reflection function at 2.16 μm , in contrast, is largely sensitive to r_e , with the largest values of the reflection function occurring for small particle sizes. In fact, as the optical thickness increases ($\tau_c \gtrsim 12$), the sensitivity of the nonabsorbing and absorbing channels to ($\tau_c(0.75 \mu\text{m})$ and r_e) is very nearly orthogonal. This implies that under optically thick conditions we can determine the optical thickness and effective radius nearly independently, and thus measurement errors in one channel have little impact on the cloud optical property determined primarily by the other channel.

A striking and unexpected feature of Fig. 2 is the fact that multiple solutions of τ_c and r_e are possible from simultaneous reflection function measurements at 0.75 and 2.16 μm , a feature that becomes increasingly pronounced as r_e and τ_c decrease. Fig. 2 also shows that the maximum reflection function at 2.16 μm generally occurs for an effective radius between 2 and 4 μm , depending on optical thickness. A comprehensive discussion of these multiple solutions, as well as a description of the effects of vertical inhomogeneity on the determination of τ_c and r_e , can be found in Nakajima and King [58]. The effective radius determined by the above procedure corresponds to the droplet radius at some optical depth within the cloud layer. For clouds having $\tau_c \gtrsim 8$, the effective radius determined using the 0.75 and 2.16 μm channels can be regarded as 85–95% of the radius at cloud top, which corresponds in turn to an optical depth 20–40% of the total optical thickness of the cloud layer. In the

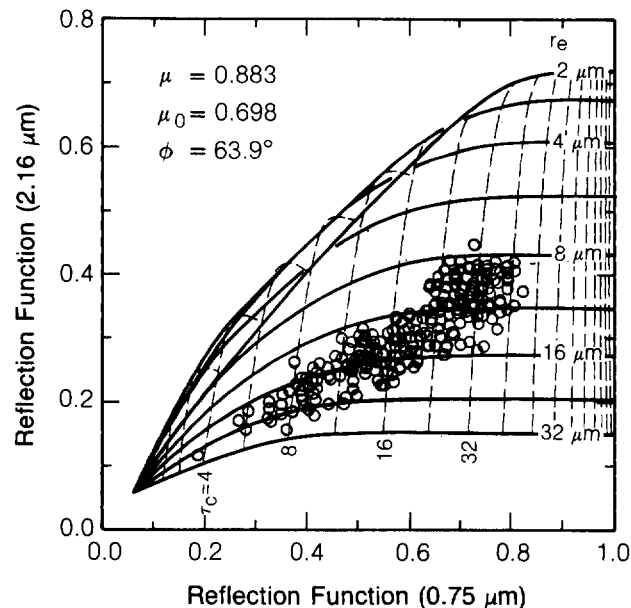


Fig. 2. Theoretical relationships between the reflection function at 0.75 and 2.16 μm for various values of the cloud optical thickness (at $\lambda = 0.75 \mu\text{m}$) and effective particle radius for the case when $\theta_0 = 45.7^\circ$, $\theta = 28.0^\circ$ and $\phi = 63.9^\circ$. Data from measurements above marine stratocumulus clouds during FIRE are superimposed on the figure (July 10, 1987) [58].

following paragraphs, we briefly describe some results of the first application of this method to experimental observations of reflected solar radiation obtained from the NASA ER-2 aircraft during the FIRE marine stratocumulus experiment, conducted off the coast of southern California during July 1987 (see Albrecht *et al.* [2] for a detailed description of this experiment).

On July 10, the ER-2 and the University of Washington C-131A flew a tightly coordinated mission in which the ER-2 flew above and the C-131A within an extensive marine stratocumulus cloud layer located approximately 355 km southwest of Coronado Island, San Diego, CA. Fig. 3 illustrates corresponding images of the cloud optical thickness τ_c and effective particle radius r_e derived from MCR measurements acquired between 0939 and 0951 PDT [59]. In both of these images, the aircraft was flying from top to bottom down the center of the images with the maximum scan of the radiometer extending up to 45° on either side of nadir (90° aperture). The data points superimposed on Fig. 2 were obtained on the left-hand side of the aircraft ($\theta = 28^\circ$) at a cross-track distance of 26.8 km (cf. Fig. 3). Both of the images in Fig. 3 were remapped to a horizontal grid at 1 km altitude, thus providing a uniform spatial scale over the 140 km \times 35 km size of the images. Analyses of this type will be performed with MODIS-N, where we will make further use of channels centered at 1.65, 3.75, and 8.55 μm . The algorithm that has been developed thus far [58] makes use of table look-up procedures and spline interpolation of multiple scattering calculations for $\tau_c < 8$ and analytic interpolation of asymptotic theory formulae for $\tau_c \gtrsim 8$.

Fig. 4 compares the retrieved effective radius with *in situ* values obtained along the nadir track of the ER-2 aircraft as a function of flight distance. The remote sensing values of

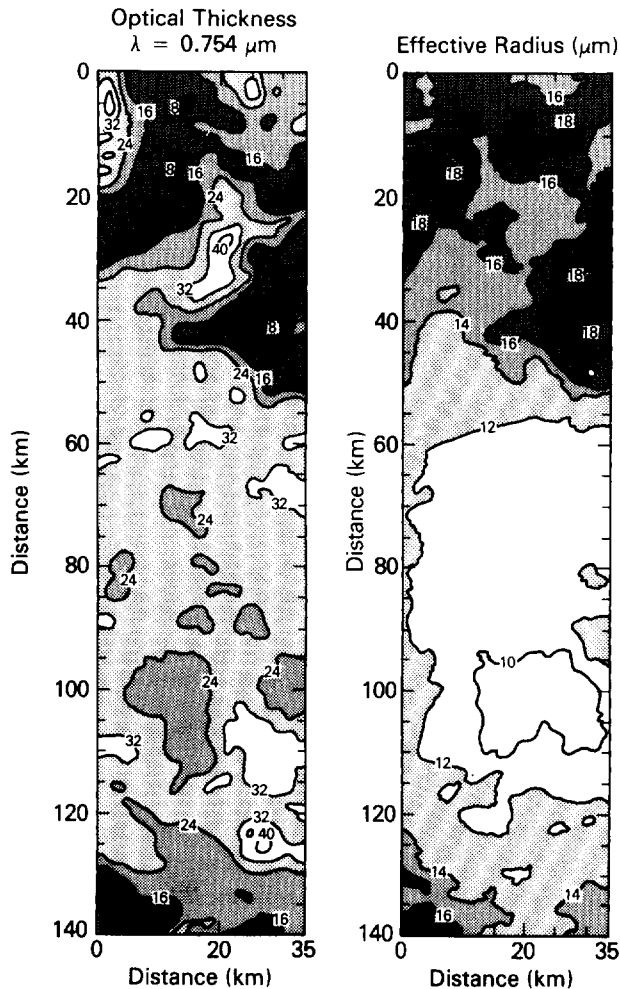


Fig. 3. Images of the cloud optical thickness and effective radius derived from 2465 scan lines of the MCR on July 10, 1987. These images have been remapped onto a horizontal grid at 1-km altitude, roughly corresponding to the cloud top altitude of the clouds in the scene [59].

effective radius r_{remote} (dashed line) have been adjusted to the expected values at the geometric center of the cloud deck r_{center} (solid line) using the method described by Nakajima and King [58]. The center-adjusted values of effective radius should be compared with the *in situ* values r_{insitu} (solid circles) derived from the Particle Measuring Systems, Inc. (PMS) probes aboard the C-131A aircraft, which was primarily flying in the middle of this 440-m thick stratocumulus cloud layer.

One of the most striking features of Fig. 4 is the very good spatial correlation between r_{center} and r_{insitu} . In general, these results show that the center-adjusted effective radius is similar in shape but noticeably larger in magnitude than corresponding values derived from *in situ* microphysical measurements. This is especially true in the central portion of the flight line where the effective radius is the smallest and the optical thickness the largest. In this region differences of up to $2.5 \mu\text{m}$ occur between the center-adjusted and *in situ* values of r_e . Twomey and Cocks [93] and Rawlins and Foot [73] also report a tendency for remote sensing to overestimate the *in situ*-derived effective radius, in the

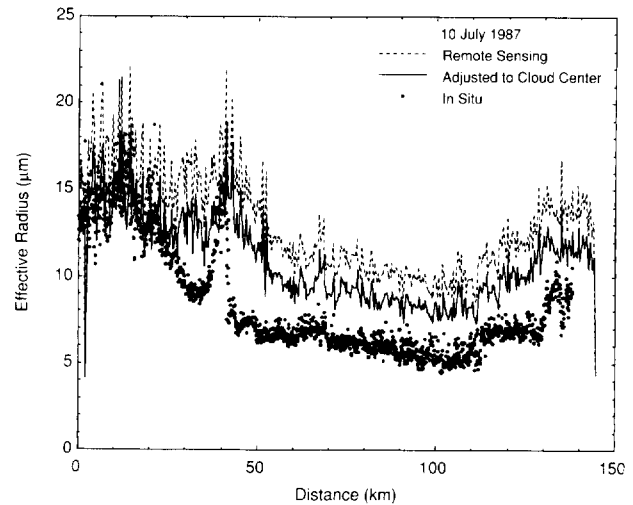


Fig. 4. Comparison of the effective radius as a function of distance along the nadir track of the ER-2 as derived from remote sensing (dashed line) and *in situ* measurements (solid circles). The solid line represents the expected values of effective radius at the geometric center of the cloud layer, derived from the remote sensing measurements by allowing for vertical inhomogeneity of droplet radius [59].

former case by 40% and in the latter case, which pertains to the FIRE marine stratocumulus region, by 20%. Nakajima *et al.* [59] suggest that the systematic overestimation of r_e by all of these investigators is due to their neglect of any water vapor continuum absorption in the 1.6 and $2.2 \mu\text{m}$ windows of the near-infrared. This suggests the urgent need to make laboratory measurements and thereby establish the extent of any water vapor continuum absorption in this important wavelength region.

At $3.75 \mu\text{m}$ the intensity received at a satellite is affected both by scattering of sunlight (during the day) and by thermal emission. Arking and Childs [4] were the first to use this channel of the Advanced Very High Resolution Radiometer (AVHRR) on the NOAA operational satellites to simultaneously infer the optical thickness and a combination of particle radius and thermodynamic phase of clouds. Nakajima and King [58] further showed that the additional information provided by a reflectance measurement at $3.75 \mu\text{m}$ substantially eliminates the multiple solutions obtained when clouds are optically thin and contain small particles (cf. Fig. 2).

Ackerman *et al.* [1] recently suggested another method for detecting optically thin cirrus clouds and of identifying their effective particle size using thermal emission measurements at 8.55, 11.0, and $12.0 \mu\text{m}$. The $8.55\text{-}\mu\text{m}$ band is centered on a weak water vapor absorption line whereas the 11.0 and $12.0\text{-}\mu\text{m}$ bands are in an atmospheric window largely unaffected by water vapor absorption lines. Their method is based on observations obtained from the High-resolution Interferometer Sounder (HIS) flown on the ER-2 aircraft during the FIRE cirrus experiment. These observations show that the blackbody brightness temperature at $8.55 \mu\text{m}$ ($T_{8.5}$) generally exceeds that at $11.0 \mu\text{m}$ (T_{11}) over optically thin cirrus clouds, but is less over clear sky regions. In contrast, the brightness temperature difference $T_{11} - T_{12}$ is generally positive both for cirrus clouds and the surface. This is illustrated in Fig. 5,

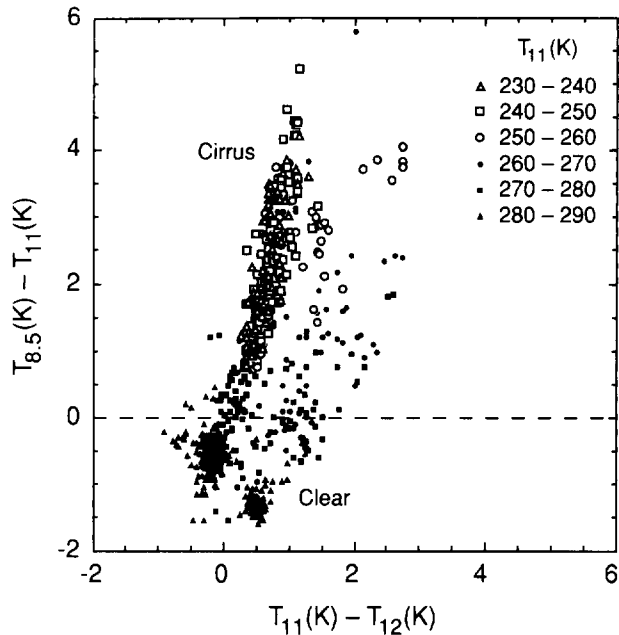


Fig. 5. HIS observed brightness temperature differences between 8.5 and 11 μm as a function of the corresponding brightness temperature differences between 11 and 12 μm [1].

which shows a scatter diagram of $T_{8.5}-T_{11}$ as a function of $T_{11}-T_{12}$. Each symbol in this figure represents a range in T_{11} as noted in the legend. Comparisons of these measurements with theory (not illustrated) generally show that the largest brightness temperature differences $T_{8.5}-T_{11}$ are associated with the smallest particle sizes, thereby providing a useful means of identifying cirrus clouds and of sizing the ice crystals contained within them.

Finally, this method of using the brightness temperature difference between 8.55 and 11.0 μm to identify the size of small particles in cirrus clouds augments and extends the corresponding method based solely on the brightness temperature difference between 10.8 and 12.6 μm , which Prabhakara *et al.* [63] showed to be the largest when the (infrared) cloud optical thickness $\tau_c \simeq 1$ and the particles have an effective radius $r_e \simeq 3\mu\text{m}$ (cf. Fig. 6). This method is applicable to water clouds as well as to ice clouds, but works the best when the temperature contrast between an optically thick cloud layer and the earth's surface is large. Fig. 7 illustrates a series of airborne HIS spectra obtained over various scenes in the 11-m window region, showing once again that the magnitude and "droop" ($T_{11}T_{12}$) in brightness temperature are both quite sensitive to the presence of optically thin cirrus clouds. Further examples of infrared emission spectra of cirrus clouds obtained from the Nimbus 4 Interferometer Spectrometer (IRIS) can be found in Prabhakara *et al.* [64].

B. Thermodynamic Phase

A relatively minor addition to the Nakajima and King [58] algorithm described above is an extension to the problem of identifying the thermodynamic phase of clouds (ice vs. water) and of distinguishing clouds from snow surfaces. More specifically, an application of their bispectral and multispectral

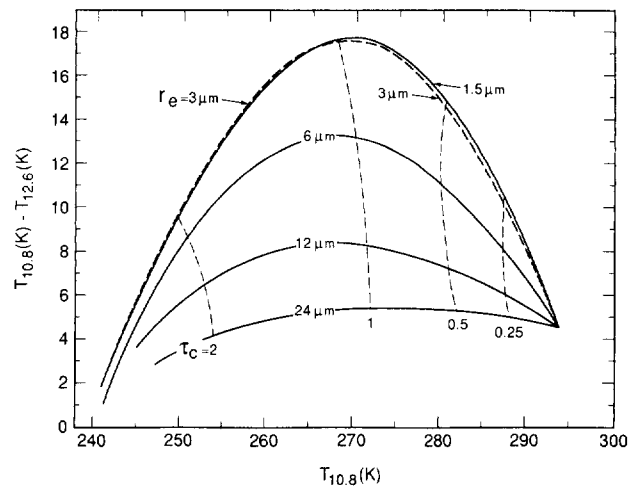


Fig. 6. Theoretical brightness temperature differences between 10.8 and 12.6 μm as a function of the corresponding brightness temperature at 10.8 μm for high-level (cirrus) spherical ice crystal clouds as a function of effective radius and optical thickness [63].

methods should yield the same, or nearly the same, particle radius if the cloud layer is composed of water. If the cloud is composed of ice or if the surface is snow covered (similar in effect to large ice particles), then the two algorithms should give dramatically different results. This technique will be incorporated in the above algorithm and tested using airborne multispectral scanning radiometer measurements in the vicinity of arctic stratus clouds overlying sea ice that were obtained over the Chukchi and Beaufort Seas during June 1990. The University of Washington C-131A aircraft utilized for this experiment contained a multispectral Cloud Absorption Radiometer (CAR) with 13 narrowband near-infrared spectral channels, including ones at 0.50, 1.64, and 2.29 μm [50]. Further demonstrations of the application of this method to the problem of distinguishing the thermodynamic phase of clouds can be found in Hansen and Pollack [33], Curran and Wu [17], and Pilewskie and Twomey [60], [61].

As an example of the sensitivity of the 1.64 μm channel of MODIS-N to the thermodynamic phase of clouds, Fig. 8 illustrates a scatter plot of the ratio of the reflection function at 1.63 μm to that at 0.75 μm as a function of the brightness temperature at 10.8 μm . These observations were obtained in central Oklahoma on June 8, 1979 as part of a NASA WB-57F airborne experiment over a cold front, and were obtained with the MCR [18], [47]. The dashed lines in this figure represent the range of the reflection function ratio to be expected for optically thick water and ice clouds at the observed solar zenith angle $\theta_0 = 29.6^\circ$, where the upper line in each pair corresponds to small particles and the lower line to large particles. This figure clearly shows that the cold portion of the scene contained ice particles whereas the warm portion contained water droplets, as expected. Although the ice portion of this cloud scene was optically thick and horizontally extensive, the water cloud was optically thinner, resulting in the reflectance ratio for the water portion of this scene being somewhat higher than theoretical calculations for a semi-infinite cloud.

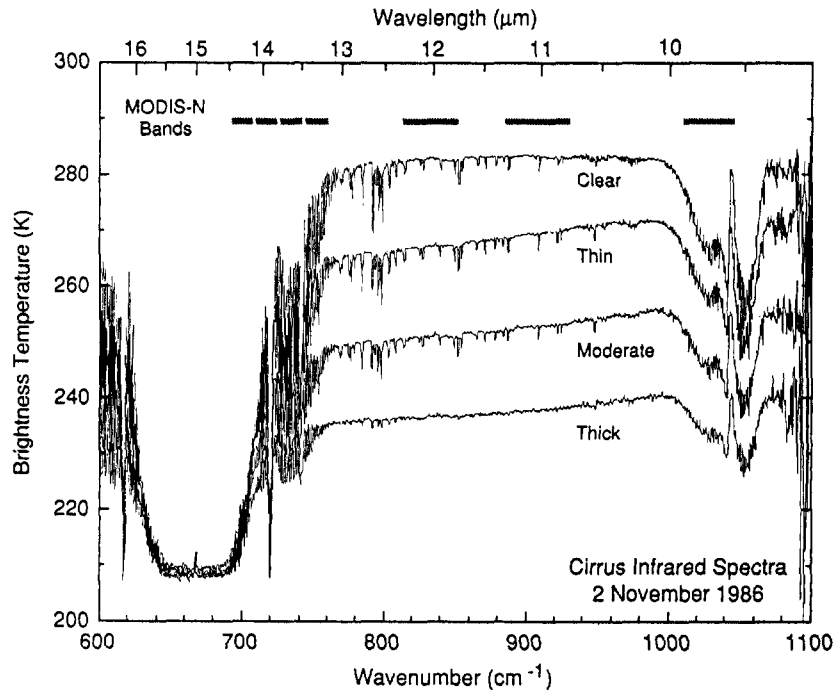


Fig. 7. HIS brightness temperature spectrum obtained between 600 and 1100 cm^{-1} (9.1 and 16.7 μm) over clear scenes and optically thin, moderate, and thick cirrus clouds during the FIRE cirrus experiment. The location and bandwidth of MODIS-N bands 30–36 are also shown in the figure.

In addition to the spectral characteristics of reflected and emitted radiation over cloud and snow-covered surfaces, Ebert [19], [20] and Welch *et al.* [98] have shown that textural features (spatial patterns) can be extremely useful for distinguishing clouds from snow or sea ice surfaces and water clouds from ice clouds. This is especially important in polar regions where the contrast between clouds and snow or sea ice surfaces is particularly low at visible and thermal infrared wavelengths. Furthermore, Welch *et al.* [97] demonstrated that it is sufficient to determine the textural features of cloud and snow-covered scenes using satellite measurements with a spatial resolution of 500 m, available from MODIS-N for a number of wavelengths $\leq 2.13 \text{ } \mu\text{m}$, since cloud classification accuracies over polar regions do not appear to increase significantly when higher spatial resolution data are employed.

C. Cloud Top Pressure and Temperature

Infrared sounder methods for determining the cloud top pressure and temperature are based on the principle that CO_2 is a uniformly mixed gas with moderate to strong absorption characteristics in the 4.3 and 15 μm thermal emission regions. Depending on the precise wavelength location of the channel, the partial CO_2 absorption is different, with each channel having its greatest sensitivity at a different level of the atmosphere. Clouds appear in the CO_2 images according to their level in the atmosphere; low clouds appearing only in the low-level channel while high clouds appear in all channels. Fig. 9 illustrates the weighting functions for the cloud retrieval channels of MODIS-N, where the weighting functions are defined as $dt(\nu, p)/d \ln p$, with $t(\nu, p)$ representing the trans-

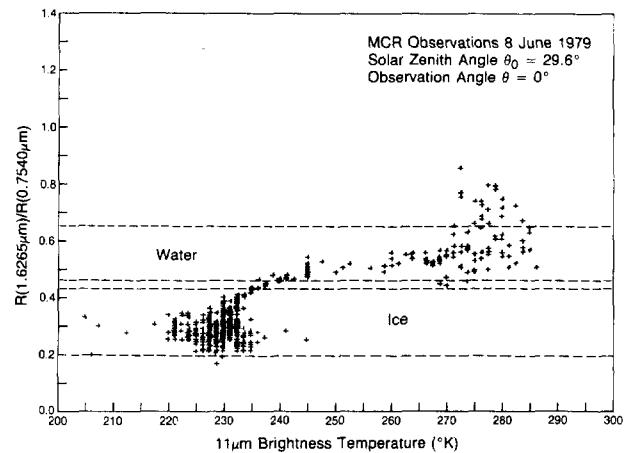


Fig. 8. Reflection function ratio $R^{1.626}/R^{0.754}$ as a function of the corresponding brightness temperature at 10.8 μm for nadir observations of the MCR over a cloud scene containing some water clouds and some ice clouds (June 8, 1979). Theoretical calculations of the range of the reflection function ratio expected for optically thick water and ice clouds of varying particle sizes are shown for comparison.

mission between atmospheric pressure level p and the satellite (at pressure $p = 0$), and ν is the frequency (wavenumber) of the channel. These functions vary slightly with different temperature and water vapor profiles. From this figure we see that channel 36 (14.24 μm) is the most sensitive to high clouds and channel 33 (13.34 μm) to low clouds, with channels 31 (not shown) and 32 (12.02 μm) located in the atmospheric window region and thus the most sensitive to the earth's surface.

Many different schemes have been developed for estimating cloud top pressure and temperature using the infrared sounding

channels of HIRS (the High-resolution Infrared Radiation Sounder) and VAS (the VISSR Atmospheric Sounder, where VISSR denotes the Visible and Infrared Spin Scan Radiometer). In the intensity ratioing method, also known as the "CO₂ slicing method" [53], [84], [54], the cloud top pressure p_c of an individual pixel is determined from a ratio of the differences in the measured intensity and a corresponding intensity for clear sky at two neighboring wavelengths. The ratio of the cloud effect in two neighboring channels can be written as

$$G^{ij}(p_c) = \frac{I^i - I_{cs}^i}{I^j - I_{cs}^j} \quad (5)$$

where I^i is the measured intensity and I_{cs}^i the clear sky intensity at frequency ν_i . This function can also be evaluated from the infrared radiative transfer equation which can be written in the form [101], [54]

$$\begin{aligned} G^{ij}(p_c) &= \frac{\epsilon^i [I_c^i(p_c) - I_{cs}^i]}{\epsilon^j [I_c^j(p_c) - I_{cs}^j]} \\ &= \frac{\epsilon^i \int_{p_s}^{p_c} t(\nu_i, p) \frac{dB^i[T(p)]}{dp} dp}{\epsilon^j \int_{p_s}^{p_c} t(\nu_j, p) \frac{dB^j[T(p)]}{dp} dp} \quad (6) \end{aligned}$$

where ϵ^i is the cloud emissivity, $I_c^i(p_c)$ the intensity that would result at frequency ν_i for a completely overcast, semi-infinite pixel, p_s the surface pressure, and $B^i[T(p)]$ the Planck function at frequency ν_i and temperature $T(p)$. An important aspect of this technique is the fact that $G^{ij}(p_c)$ is independent of the fractional cloud cover within the pixel. Choosing two channels near one another permits the further assumption that $\epsilon^i = \epsilon^j$. Fig. 10 illustrates the cloud top pressure function $G^{ij}(p_c)$ calculated from (6) under varying assumptions on the vertical distribution of temperature and moisture. These calculations are based on channels 6 and 7 ($\nu_i = 733 \text{ cm}^{-1} = 13.64 \text{ } \mu\text{m}$, $\nu_j = 749 \text{ cm}^{-1} = 13.25 \text{ } \mu\text{m}$) of HIRS-2, which correspond closely to channels 34 and 33 of MODIS-N, respectively. The midlatitude atmosphere has a steeper slope (and hence less sensitivity to pressure) than the tropical atmosphere. For an isothermal atmosphere the slope is infinite and thus no cloud top pressure information can be retrieved from CO₂ sounder channels. Except in polar regions, where low-level temperature inversions are common in winter, a measurement of $G^{ij}(p_c)$ can readily be used to determine p_c .

When utilizing more than two frequencies for cloud top pressure determination, as will be the case for MODIS-N, alternative statistical methods have been developed which are generally referred to as "minimum residual methods" [11], [54], [89], [21]. Wielicki and Coakley [101] showed that these methods are equivalent to the intensity ratioing method when using only two channels, but that these methods differ somewhat from each other in the statistical measure to be minimized when more than two channels are utilized. One of the distinct advantages of MODIS-N over HIRS-2 is the better spatial resolution of the channels (1 km footprint as opposed

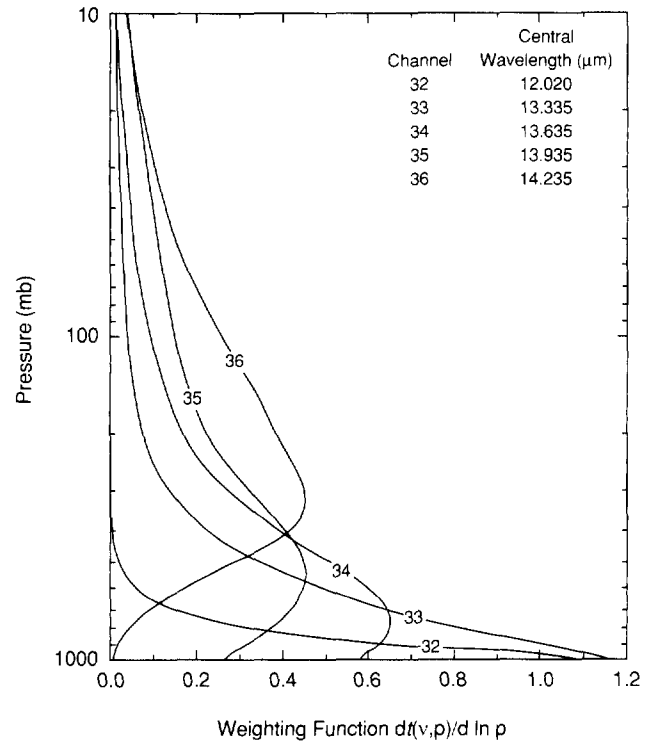


Fig. 9. Weighting functions $[dt(\nu, p)/d \ln p]$ as a function of pressure for the MODIS-N cloud infrared sounder channels.

to 25 km). This will substantially increase the proportion of fully cloud-filled fields of view that will be detected, in comparison with what is currently possible from routine satellite observations.

Smith and Frey [83] recently investigated the accuracy of cloud top pressures determined using the CO₂ slicing and minimum residual methods, where both methods were applied to HIS spectra obtained from the high-altitude ER-2 aircraft (cf. Fig. 7). The cloud top pressures thus obtained were compared to comparable results obtained from nearly simultaneous airborne lidar observations [86], [1]. These comparisons showed that the two-channel and minimum residual methods, when applied to HIS spectra degraded to a spectral resolution comparable to that of the MODIS-N sounder channels (channels 33–36), lead to cloud top pressures determined to an accuracy of 36 and 31 mb, respectively.

Once the cloud top pressure has been determined for a given pixel, the cloud top temperature may readily be determined from the temperature profile to be obtained by inversion of nearly coincident measurements from the Atmospheric Infrared Sounder (AIRS). Although temperature profiles in the lower atmosphere can also be estimated from MODIS-N, the lower spectral resolution of MODIS-N makes the temperature soundings highly dependent on a reliable first guess profile. Furthermore, AIRS has higher spectral resolution and will make direct use of microwave sounding measurements to be obtained with the Advanced Microwave Sounding Unit-A (AMSU-A) and Microwave Humidity Sensor (MHS), making its determination of the complete temperature and moisture profile preferable for this and other applications.

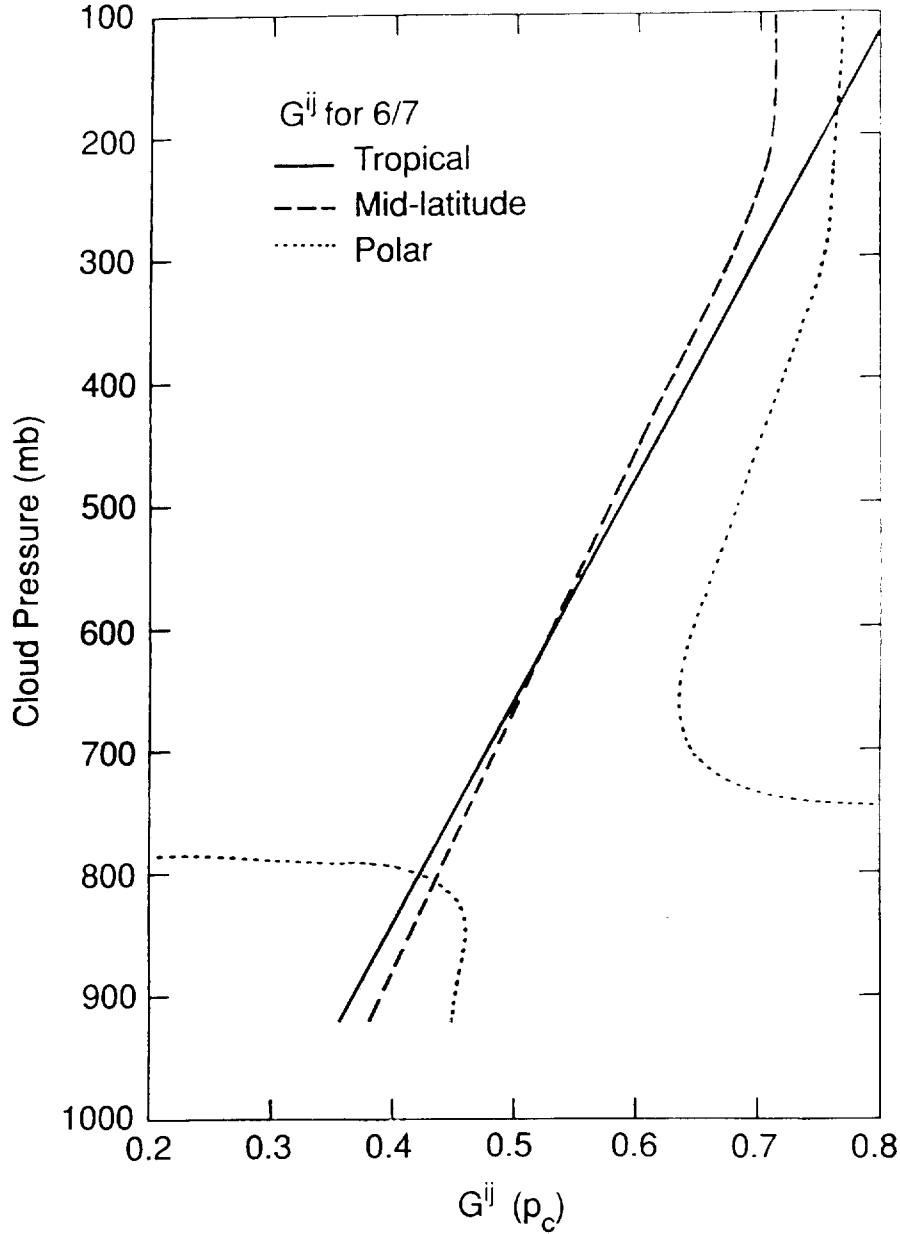


Fig. 10. Cloud top pressure function $G^{ij}(p_c)$ calculated for channels 6 and 7 ($\nu_i = 733\text{cm}^{-1} = 13.64\mu\text{m}$, $\nu_j = 749\text{cm}^{-1} = 13.25\mu\text{m}$) of HIRS-2 using tropical, midlatitude, and polar climatological temperature and moisture profiles [101]. These channels correspond closely to channels 34 and 33 of MODIS-N, respectively.

The algorithms presented above assume the presence of a single cloud layer within the instantaneous field of view of the radiometer. When multiple cloud layers are present some errors in the derived cloud top pressure are introduced, though the high spatial resolution of MODIS-N should reduce these effects somewhat. Multilayer cloud systems in which the upper layer cloud is semitransparent and the underlying cloud is opaque will lead to an overestimation of the cloud top pressure (underestimate of the cloud top altitude) of the semitransparent cloud by < 100 mb. The bias error in the derived cloud top pressure of the semitransparent cloud is the greatest when the underlying opaque cloud is in the middle troposphere (400–700 mb) and small to negligible when the opaque cloud is near the surface or near the semitransparent cloud layer [55].

D. Cloud Effective Emissivity

Once the cloud top temperature and pressure have been determined, it is possible to determine the cloud effective emissivity (also known as the effective fractional cloud cover) of the pixel [105]. This may be accomplished by noting that the emitted intensity of a partially cloud-filled scene in the infrared window region can be expressed as

$$\begin{aligned} I^w &= (1-f)I_{cs}^w + f[(1-\epsilon^w)I_{cs}^w + \epsilon^w B^w(T_c)], \\ &= f\epsilon^w B^w(T_c) + (1-f\epsilon^w)I_{cs}^w \end{aligned} \quad (7)$$

where w denotes the window channel frequency, f the fractional cloud cover, $B^w(T_c)$ the Planck function at cloud top temperature T_c , and I_{cs}^w the infrared window intensity observed under clear sky conditions. This expression clearly

demonstrates that the infrared intensity over a partially filled field of view is a function of the effective emissivity $f\epsilon^w$ and not the fractional cloud cover f or cloud emissivity ϵ^w separately. Rewriting this expression leads to the following expression for the effective emissivity:

$$f\epsilon^w = \frac{I^w - I_{cs}^w}{B^w(T_c) - I_{cs}^w} \quad (8)$$

an expression that was used previously in deriving (6) from (5). Using the high spatial resolution visible and near-infrared measurements available from MODIS-N, f can be directly inferred (see below), thereby permitting the emissivity ϵ^w to be derived.

Alternative methods have been proposed for inferring the effective emissivity from differences in the brightness temperature between the 11 and 12- μm window channels [104]. These methods make use of the fact that the brightness temperature difference between 11 and 12 μm is small when the emissivities are near unity, such as occurs for clear skies and optically thick clouds, but is positive for optically thin clouds with emissivities less than unity (cf. Figs. 6 and 7). In addition to effective emissivity, this temperature difference is sensitive to cloud top temperature and effective particle size [63], [104].

Finally, in the case of multilayer cloud systems in which the upper layer cloud is semitransparent and the underlying cloud is opaque, the error in effective emissivity increases as the underlying cloud layer approaches the altitude of the semitransparent cloud, with the effective emissivity assumed to be unity when the two layers coincide. As a result, the effective emissivity derived from the above technique is likely to be somewhat overestimated in the presence of multiple cloud layers [55].

E. Fractional Cloud Cover

There are two major reasons for determining cloud cover using MODIS-N observations. The first is to provide a cloud detection mask for the purpose of avoiding cloud contamination in the determination of surface properties such as vegetation. For this purpose, the desire is to avoid any possible cloud contamination, including the effects of cloud shadows. Pixels flagged as being clear are, therefore, only those which have a high probability of being clear, unshadowed fields of view. The second reason is to ascertain which data are appropriate for determining cloud physical and radiative properties. For this purpose, an unbiased estimate of cloud cover is desired. An example of this latter use is for studies of the effects of clouds on the earth's radiation budget.

For cases of large-scale cloudiness (e.g., boundary layer stratus), the distinction between clear and cloudy scenes is relatively straightforward during the day, but difficult at night. For cases involving optically thin cloud (e.g., cirrus), large aerosol amount, or clouds over snow and sea ice surfaces, the distinction can be rather difficult. Since there are numerous criteria that can be applied for the identification of "clouds," the MODIS-N processing system will apply a multiplicity of algorithms, each of which will succeed in some cloud climatological regimes and likely fail in others. Prior to the

implementation of these criteria, the "darkest" and "warmest" values of channels 1 (0.66 μm) and 32 (12.02 μm), respectively, for each geographic region will be determined from measurements obtained during the previous week. These measurements will be used as the expected clear-sky values for the current measurement, in a manner analogous to that described by Rossow *et al.* [78], [77]. With an estimate of the clear-sky scenes for each geographical region thus obtained, the MODIS cloud identification criteria will consist of, but will not be limited to, the following:

Shortwave threshold—the reflection function defined in (1) will be computed for channel 1 of MODIS-N and compared to the "darkest," clear-sky, reflection function for that region from the previous week. If the measured reflection function exceeds the clear-sky estimate by some amount (e.g., 0.03 over oceans), the pixel is presumed to be cloud, aerosol, or snow contaminated. This threshold will not be applied to sunglint regions of the open ocean where the clear sky reflectance may exceed that from cloudy scenes.

Longwave threshold—the brightness temperature at 12.02 μm will be computed from channel 32 of MODIS-N and compared to the "warmest," clear-sky, brightness temperature for that region from the previous week. If the measured brightness temperature is less than the clear-sky brightness temperature by some threshold (e.g., 3K over oceans), the pixel is suspected of being cloud or snow contaminated.

Bispectral threshold—in this method, a combination of the shortwave and longwave threshold methods, a pixel is considered cloudy if the reflection function at 0.66 μm exceeds the clear-sky estimate by 0.03 or greater or the brightness temperature at 12.02 μm is colder than the clear-sky estimate by 3K or more. This method is similar to that used to identify clouds in the International Satellite Cloud Climatology Project (ISCCP) [78], [76]. This algorithm has the greatest difficulty distinguishing optically thick marine stratocumulus clouds at night, optically thin cirrus clouds, and clouds from snow and sea ice surfaces.

Hybrid bispectral threshold—similar but more complex than the bispectral threshold method in that this method attempts to account for partially filled fields of view. Furthermore, this method provides an estimate of whether the clouds are low, middle, or high (see Minnis and Harrison [56] for further details).

Spatial coherence—this is an infrared method only, which relies on the spatial variability within the cloud field to determine cloud cover (see Coakley and Bretherton [15] for details). Spatial coherence assumes only that the cloud field occurs in layers and that the clouds are optically thick in the infrared window. It is particularly useful for identifying single and multilevel cloud layers over oceanic regions.

We envision a cloud screening and identification algorithm similar to the ones developed by Saunders [79], Saunders and Kriebel [80], Stowe *et al.* [88], and Gutman [31]. In each one of these methods, multiple tests such as the ones described above are applied. Furthermore, we anticipate making use of MODIS-N measurements at 1.64 and 8.55 μm to aid in the discrimination of snow from clouds and for identifying the presence of optically thin cirrus clouds with emissivities

less than unity. Over land, we envision making use of additional measurements in the 0.94- μm water vapor band which, together with measurements in the nearby 0.87- μm window region, should prove invaluable in helping to discriminate clouds having little overlying water vapor absorption from dark shadows and bright surface features [29]. Finally, texture measures will be utilized for distinguishing clouds from snow and sea ice in polar regions [19], [20], [98]. The accuracy and sensitivity to spatial resolution of each of the above specified methods has recently been assessed by Wielicki and Parker [102] based on Landsat Thematic Mapper (TM) data acquired over 24 ocean scenes. They concluded that the accuracy of fractional cloud cover estimates derived from satellite sensors degrades considerably as the spatial resolution of the sensor increases above 250 m.

V. AEROSOL PROPERTIES

In deriving aerosol properties from MODIS-N data, only those pixels that have been identified as being cloud free will be utilized. We anticipate that the cloud-screening algorithm described above will result in several subpixel clouds and optically thin low clouds being undetected. It is difficult to assess, at this early stage, the exact impact that these residual clouds will have on the retrieval of aerosol properties. However, due to the 250-m spatial resolution of MODIS-N at 0.66 and 0.87 μm , we expect that these effects will be much smaller than in earlier analyses of satellite data [22], [27], [42], [43], [45]. These effects can further be reduced by observing the spatial distribution of the derived aerosol optical thickness, inasmuch as aerosols vary less rapidly with distance than do clouds. Derivations of particle size can also be used to examine the effects of cloud contamination, since cloud droplets are generally $\gtrsim 6 \mu\text{m}$ in radius, whereas smoke and anthropogenic aerosol particles tend to be submicron in size (0.2–0.4 μm) [67], [100]. Dust particles are generally larger (1–3 μm) than the bulk of the aerosol particles in the atmosphere, and thus their size is more difficult to distinguish from that of cloud droplets.

In the following sections we will describe methods for determining the aerosol optical thickness, mean particle size (or, in some instances, the size distribution), single scattering albedo, and mass loading. We will also describe a hybrid method for deriving all of these parameters simultaneously from a given set of images. The advantage of the hybrid method is that it does not depend on an *a priori* estimate of the particle size and single scattering albedo in order to derive aerosol optical thickness, relying instead on extrapolating these values from parts of the image where they can be derived. Each of these parameters, however, can best be determined under specific observing conditions. Aerosol optical thickness, for example, can be derived the most accurately over terrain having a dark surface [27], [42] or in which there are sharp contrasts [91]. The size distribution can be derived only over very dark surfaces (water or dense dark vegetation) when the aerosol optical thickness is large ($\gtrsim 0.2$) [43]. The aerosol single scattering albedo requires even larger optical thickness ($\gtrsim 0.5$) [22] and can be derived over scenes having a strong

spatial [40] or spectral contrast [43]. The hybrid method requires that all of these conditions be met simultaneously in the images that are analyzed. In the following subsections we will describe each of these techniques in further detail. Finally, the implementation of these methods to MODIS-N observations will be described.

A. Spectral Aerosol Optical Thickness

Methods for deriving the aerosol optical thickness can be classified into two categories: (1) methods that derive the absolute optical thickness from reflection function measurements in a single image, and (2) methods that derive the difference in the optical thickness between consecutive images taken over the same geographic area. In methods of the first type, the optical thickness is derived from reflected intensity measurements over selected pixels of the image for which the surface reflectance is low (e.g., $\lesssim 0.05$), and requires further that the value of the surface reflectance be known *a priori* with high precision (e.g., clear water or dense vegetation [30], [42], [45]). In methods of the second type, the difference in the optical thickness is derived from the change in the measured contrast between selected pixels in the image [91]. The advantage of this type of method is that it can be applied over terrain where dark pixels do not exist. The disadvantage is that it is difficult to convert the resulting differences in the optical thickness into an absolute value. In order to accomplish this objective, a clear day must be selected and the value of the optical thickness for this day needs to be measured or assumed *a priori*. The decision of whether the clearest image from the set of images is really a clear day is not an easy one and is often based on a subjective inspection of the sharpness of the image or on meteorological observations of the origin of the air mass within the image. In the following paragraphs we will describe both of these methods, together with examples of their application to satellite data.

In methods of the first type the aerosol optical thickness (τ_a) can be determined in spectral bands and over surface covers that have low spectral reflectance. In the blue wavelength region of MODIS-N (0.42 and 0.47 μm), the aerosol optical thickness can be determined over vegetation, dark soils, and water bodies with low chlorophyll and low turbidity; in the red region (0.66 μm) over dark densely vegetated forests and large water bodies; and in the near-infrared (0.87, 1.24, 1.64, and 2.13 μm) over large water bodies. The reflection function of a cloud-free and vertically homogeneous earth-atmosphere system overlying a Lambertian surface with reflectance A_g can be written as [12]

$$R(\tau_a, \omega_0; \mu, \mu_0, \phi) = R_{atm}(\tau_a, \omega_0; \mu, \mu_0, \phi) + \frac{A_g}{1 - A_g \bar{r}_{atm}(\tau_a, \omega_0)} t_{atm}(\tau_a, \omega_0; \mu) t_{atm}(\tau_a, \omega_0; \mu_0) \quad (9)$$

In this expression, $R_{atm}(\tau_a, \omega_0; \mu, \mu_0, \phi)$ is the reflection function, $\bar{r}_{atm}(\tau_a, \omega_0)$ the spherical albedo and $t_{atm}(\tau_a, \omega_0; \mu_0)$ the total transmission (diffuse plus direct) when $A_g = 0$. Each of these functions is explicitly a function of aerosol optical thickness (τ_a) and single scattering albedo

(ω_0) and implicitly a function of the aerosol size distribution. The functions $\bar{r}_{atm}(\tau_a, \omega_0)$ and $t_{atm}(\tau_a, \omega_0; \mu_0)$ are equivalent to $\bar{s}(\tau_a, \omega_0)$ and $\gamma(\tau_a, \omega_0; \mu_0)$ in Chandrasekhar's [12] notation, respectively.

When the surface reflectance is small, as in the cases outlined above, the first term in this expression dominates, thus yielding sensitivity to the reflection function of the atmosphere alone. This term, in turn, is primarily a function of the aerosol optical thickness with a reduced sensitivity to aerosol size distribution and optical properties (i.e., single scattering albedo). Fig. 11 illustrates the reflection function at $0.61 \mu\text{m}$ as a function of aerosol optical thickness for an atmosphere consisting of Rayleigh (molecular) scattering ($\tau_R = 0.066$), ozone absorption ($\tau_{O_3} = 0.021$) and aerosol scattering and absorption, where the aerosol size distribution is assumed to be a Junge distribution of the form $n(r) \propto r^{-4}$ [25]. The computations presented in this figure apply to the case where $\theta_0 = 40^\circ$ and pertain to four different values of the surface reflectance ($A_g = 0.0, 0.1, 0.2$, and 0.4). Figs. 9(a) and (b) show the sensitivity of the reflection function to τ_a and A_g when $\theta = 60^\circ$ and $\phi = 0^\circ$, while Figs. 9(c) and (d) apply to nadir observations ($\theta = 0^\circ$). Figs. 9(b) and (d) illustrate conditions where the aerosol single scattering albedo $\omega_0 = 0.81$, and contrast sharply with conditions where aerosol absorption is weak ($\omega_0 = 0.96$, Figs. 9(a) and (c)). This figure clearly illustrates the principle behind the remote sensing of aerosol optical thickness over low reflectance surfaces, viz., the reflection function increases almost linearly as the optical thickness increases, and is the most sensitive for low reflectance surfaces. The slope, however, depends strongly on the aerosol optical properties as well as the solar illumination and surface reflectance conditions. Fig. 11 further demonstrates that a knowledge of the surface reflectance is required in order to reduce the uncertainties in the derived values of τ_a , and that the reflection function is less sensitive to optical thickness over bright surfaces unless the aerosol absorption is moderate to large.

Kaufman and Sendra [42] developed an algorithm for deriving the aerosol optical thickness from satellite images with at least 5% of the pixels covered with dense dark vegetation. This algorithm is based on the concept that the reflection function above a dark scene, or at a wavelength for which the surface reflectance is small, increases with optical thickness (cf. Fig. 11). In contrast, the reflection function at a wavelength having a large surface reflectance generally decreases with increasing optical thickness or at least increases less strongly. Pixels covered by dense dark vegetation can be identified in a satellite image by selecting those pixels having the largest normalized difference vegetation index (NDVI), defined for MODIS-N by

$$NDVI = \frac{R^{0.87} - R^{0.66}}{R^{0.87} + R^{0.66}}. \quad (10)$$

From this group of pixels, the fraction of pixels having the lowest reflection function at $0.66 \mu\text{m}$ is selected. Having determined the pixels overlying dark vegetation and by assuming the surface reflectance at each wavelength for these vegetated areas, the aerosol optical thickness can be determined by

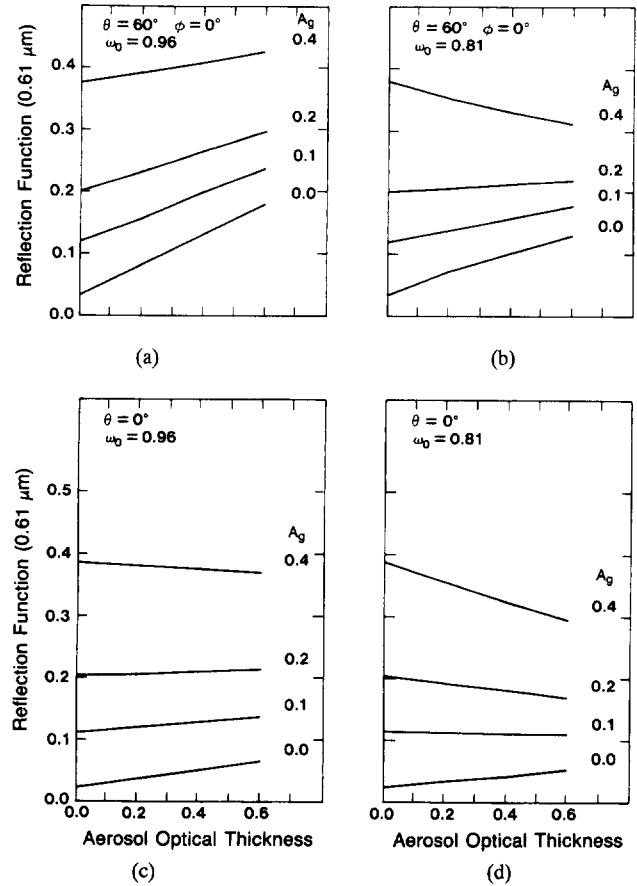


Fig. 11. The reflection function as a function of aerosol optical thickness and surface reflectance for a Junge size distribution given by $n(r) \propto r^{-4}$, where $\lambda = 0.61 \mu\text{m}$ and $\theta_0 = 40^\circ$. Panels (a) and (b) apply to the case where $\theta = 60^\circ$ and $\phi = 0^\circ$ but for different single scattering albedos; (c) and (d) to nadir observations ($\theta = 0^\circ$) [25].

applying a table look-up procedure similar in concept to the computational results presented in Fig. 11.

This method is illustrated in Fig. 12, which shows measurements of the reflection function obtained from Landsat-3 at $0.65 \mu\text{m}$ as a function of the NDVI, computed for this case using Multispectral Scanner (MSS) band 2 ($0.65 \mu\text{m}$) and band 3 ($0.75 \mu\text{m}$) measurements acquired on a clear (Fig. 10(a)) and hazy (Fig. 10(b)) day over Washington, DC and the Chesapeake Bay region in August 1982. From this figure one readily sees that the measurements having the highest vegetation index generally correspond to those pixels having the lowest reflection function at $0.65 \mu\text{m}$, and thus to the darkest vegetation regions of the scene. Fig. 13 illustrates normalized histograms of the $0.65\text{-}\mu\text{m}$ reflection functions for these two scenes before (unshaded) and after (shaded) applying the dense vegetation selection procedure outlined above.

Histograms of the aerosol optical thickness derived from satellite measurements for the selected pixels in these scenes are illustrated in Fig. 14. The derived values of optical thickness both at $0.55 \mu\text{m}$ (Fig. 12(a)) and $0.65 \mu\text{m}$ (Fig. 12(b)) are seen to agree well with nearly simultaneous measurements obtained from ground-based sunphotometer measurements, denoted by the arrows at the bottom of the figure [42]. In deriving these results the surface reflectance for the dark

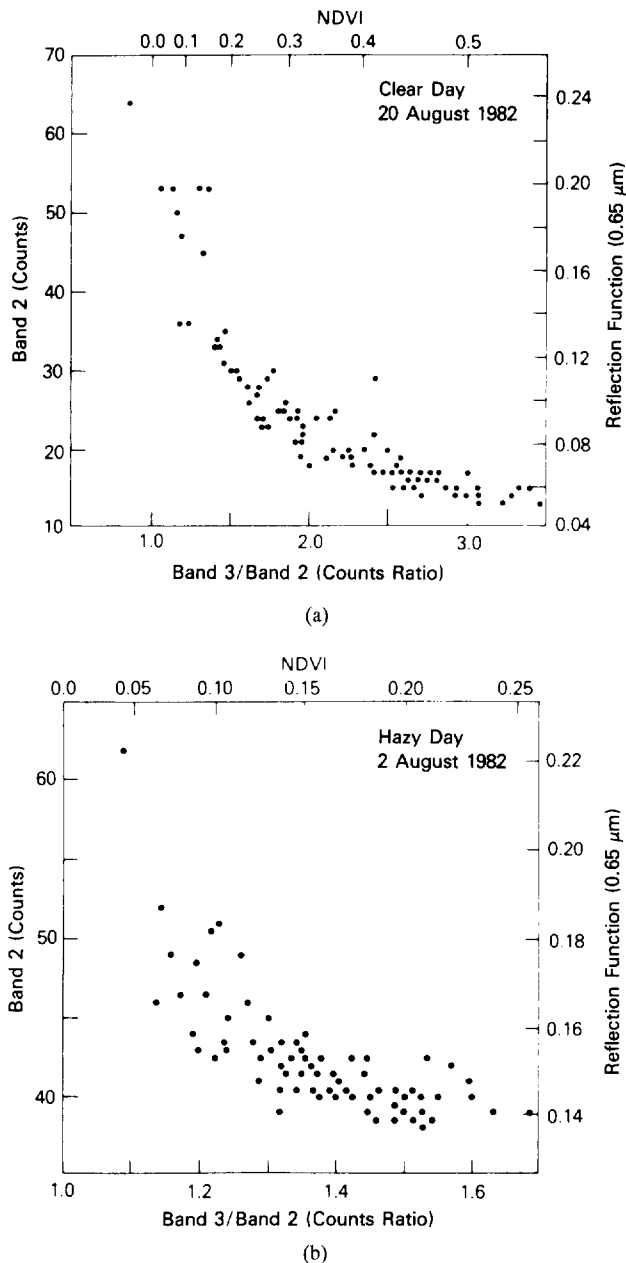


Fig. 12. Scatter diagram of the intensities and reflection functions of Landsat-3 MSS band 2 ($0.65 \mu\text{m}$) as a function of the normalized difference vegetation index (NDVI; upper scale). Each data point represents an average of 10×10 pixels, where (a) corresponds to a clear day (August 20, 1982) and (b) to a hazy day (August 2, 1982) [42].

vegetated surfaces was assumed to be 0.02 ± 0.01 at both 0.55 and $0.65 \mu\text{m}$ [42]. The haze in this case was a smoke layer located above 3 km , and was later traced to a large forest fire in Alberta, Canada that occurred a few days earlier [22].

Fig. 15 illustrates a map of the world showing large-scale regions where (a) the Kaufman and Sendra [42] algorithm is likely to be successful, (b) the accuracy of the application is uncertain, and (c) the application of the algorithm is doubtful. In addition to these land regions, the determination of the aerosol optical thickness over the ocean should be comparatively less difficult. In fact, NOAA/NESDIS has been estimating aerosol optical thickness in cloud-free regions over

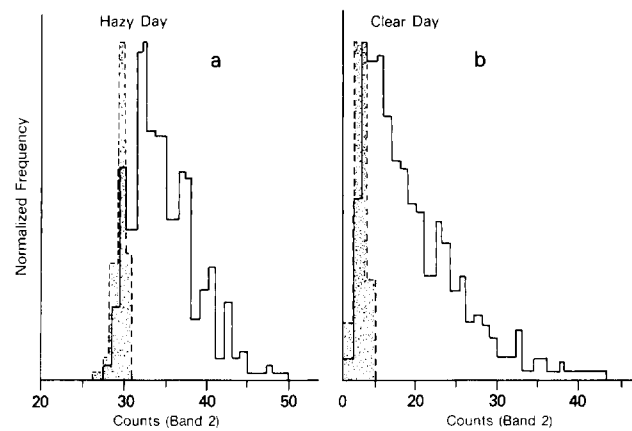


Fig. 13. Normalized histograms of the reflected intensity (in counts) from Landsat-3 MSS band 2 ($0.65 \mu\text{m}$) for (a) the hazy day (August 2, 1982) and (b) the clear day (August 20, 1982). Original histograms (unshaded) and histograms after applying the selection algorithm (shaded) are illustrated [42].

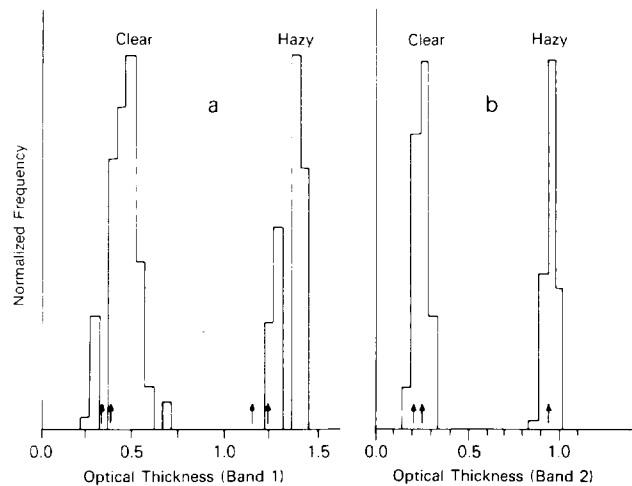


Fig. 14. Normalized histograms of the aerosol optical thickness derived from Landsat-3 MSS. (a) band 1 ($0.55 \mu\text{m}$) and (b) band 2 ($0.65 \mu\text{m}$) for the clear day (August 20, 1982) and the hazy day (August 2, 1982). The arrows show the corresponding measurements from ground-based sunphotometers [42].

the global oceans on a daily basis using AVHRR data since 1987 [71].

Finally, in regions where the surface reflectance is relatively large and dense dark vegetation is absent, as in the case of desert regions, it is sometimes possible to determine the aerosol optical thickness from the reduced contrast in a satellite image. This is demonstrated in Fig. 16, which shows Landsat-5 Thematic Mapper (TM) images obtained on 4 days during April 1986 and April and May 1987. These images, acquired in band 2 ($0.56 \mu\text{m}$), represent a $15 \times 15 \text{ km}$ region near the Atlantic coast of Senegal, Africa. They clearly demonstrate the degradation of contrast that results when the aerosol optical thickness increases from small (April 30, 1986) to large (April 17, 1987) values.

Tanré *et al.* [91] developed a method whereby the difference between the aerosol optical thickness on a clear and hazy day can be derived from the contrast deterioration between the 2 days. For this purpose Tanré *et al.* computed a structure function for the entire scene on both days, and showed that

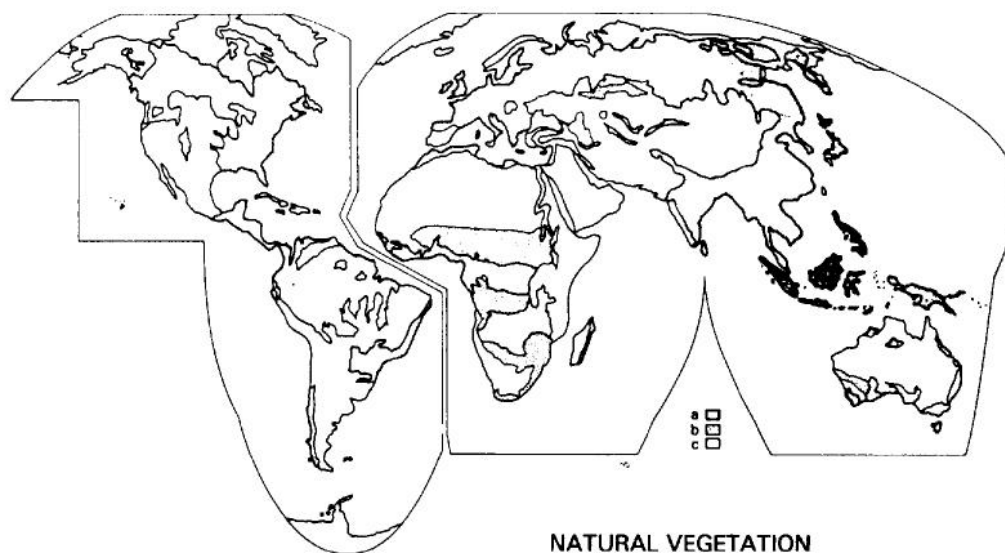


Fig. 15. Regions around the world where: (a) the dark vegetation algorithm is expected to be successful (forests with evergreen and deciduous trees as well as high shrubs), (b) there is an uncertainty in the application (same vegetation as (a) but growing in patches or singly), and (c) the successful application is unlikely (areas where trees or high shrubs, if found, grow singly) [42].

this statistic is proportional to $t_{atm}^2(\tau_a, \omega_0; \mu) t_{atm}^2(\tau_a, \omega_0; \mu_0)$. As a consequence, the structure function, and hence contrast, decreases as the optical thickness increases. This method can be understood on examination of Fig. 17, which shows histograms of the reflection function obtained on each of the days shown in Fig. 16. Each histogram is labeled with the date and aerosol optical thickness derived from nearly simultaneous ground-based sunphotometer measurements at $0.55 \mu\text{m}$. These histograms clearly demonstrate that as the optical thickness of the Saharan aerosol increases, the reflection function of the earth-atmosphere system increases while the contrast simultaneously decreases. The contrast is here represented by the narrowing of the width of the histogram as the optical thickness increases. The fact that the reflection function increases as the optical thickness increases suggests that the surface reflectance is not too great ($A_g \approx 0.15$) and that the aerosol particles are not highly absorbing, as this would lead to the reflection function decreasing, as illustrated in Fig. 11 for some observation conditions when $A_g = 0.4$. An example of an application of this method is presented in Fig. 18, which shows the spectral aerosol optical thickness derived for the 4 days shown in Figs. 16 and 17. In this figure, the solid curves correspond to satellite retrievals using Tanré *et al.*'s deblurring algorithm and the dashed curves to nearly simultaneous ground-based sunphotometer measurements.

A simpler method for deriving the aerosol optical thickness over land from spaceborne observations was developed by Fraser *et al.* [27]. In this method it is not necessary to assume either the presence of dense dark vegetation or contrast in surface reflectance within the scene, relying instead on the difference in optical thickness between subsequent scenes and the fact that the reflection function increases as the optical thickness increases, provided the surface reflectance is not large ($A_g \lesssim 0.15$). Fraser *et al.* [27] tested this method

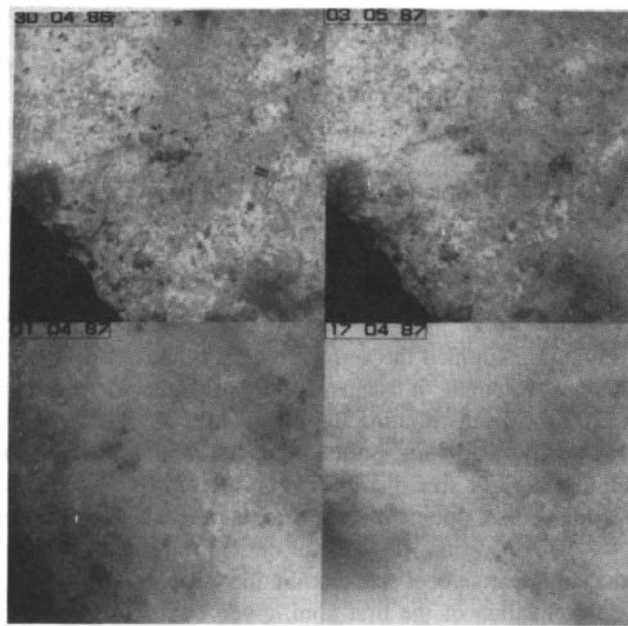


Fig. 16. Images constructed from Landsat-5 TM data in band 2 ($0.56 \mu\text{m}$) on 4 days during April 1986 and April and May 1987. These images are for a $15 \times 15 \text{ km}$ region near the Atlantic coast of Senegal, Africa, and are centered at 14.1°N latitude and 16.7°W longitude. They clearly show the degradation of contrast that results when the aerosol optical thickness increases from small (April 30, 1986) to large (April 17, 1987) values.

using VISSR measurements obtained from the GOES satellite and compared these satellite-derived aerosol optical thickness values with nearly simultaneous ground-based sunphotometer measurements obtained at several locations in the eastern U. S. Fig. 19 shows a comparison of these satellite-derived values with collocated and concurrent ground-based measurements obtained by J. Prospero of the University of Miami during the summers of 1980 and 1981. The solid line in this figure represents the best-fit regression line using all of the data, whereas

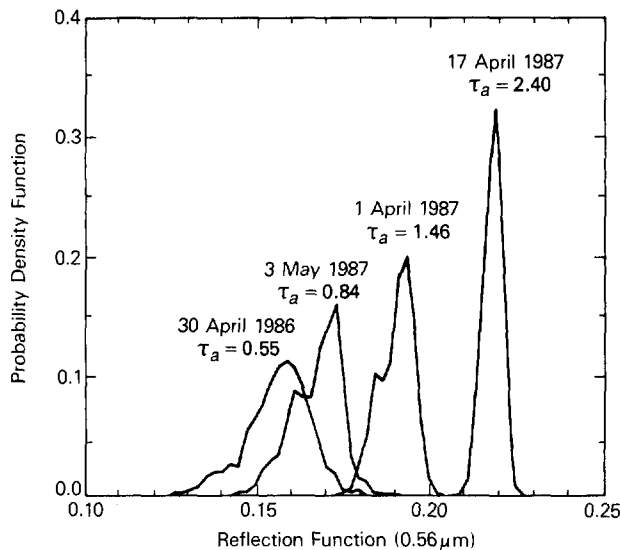


Fig. 17. Histograms of the reflection function of a region in Senegal, Africa observed by Landsat-5 TM band 2 ($0.56 \mu\text{m}$) on 4 days during 1986 and 1987. The aerosol optical thickness derived from nearly simultaneous ground-based sunphotometer observations at $0.55 \mu\text{m}$ is also indicated for each day [91].

the dashed lines represent the standard deviation of the range of regression lines that are obtained using the bootstrap method applied to 1000 random subsets of the data, thereby containing 68% of the regression lines. The average error in the satellite-derived aerosol optical thickness was $\Delta\tau_a = 0.08$, with 75% of the intercomparisons having errors < 0.1 .

B. Mean Radius and Dispersion of the Aerosol Size Distribution

Having determined the aerosol optical thickness as a function of wavelength, it is possible in principle to determine the aerosol size distribution by inversion of the linear system produced by quadrature [49], [46], [87]. In this method, the columnar aerosol size distribution is inferred by numerically inverting aerosol optical thickness measurements as a function of wavelength, where the aerosol optical thickness is related to the columnar aerosol size distribution through the Fredholm integral equation of the first kind, given by

$$\tau_a(\lambda) = \int_0^\infty \pi r^2 Q_{ext}(r, \lambda, m) n_c(r) dr. \quad (11)$$

In this expression r is the particle radius, $Q_{ext}(r, \lambda, m)$ the extinction efficiency factor, a function of size parameter $\alpha = 2\pi r/\lambda$ and refractive index m , and $n_c(r)$ the unknown columnar size distribution, that is, the number of particles per unit area per unit radius interval in a vertical column through the atmosphere.

We do not currently envision routinely inverting spectral aerosol optical thickness measurements, but instead intend to derive model log-normal size distribution parameters representing the mean radius and dispersion of the size distribution. Over oceans and under certain viewing and solar illumination

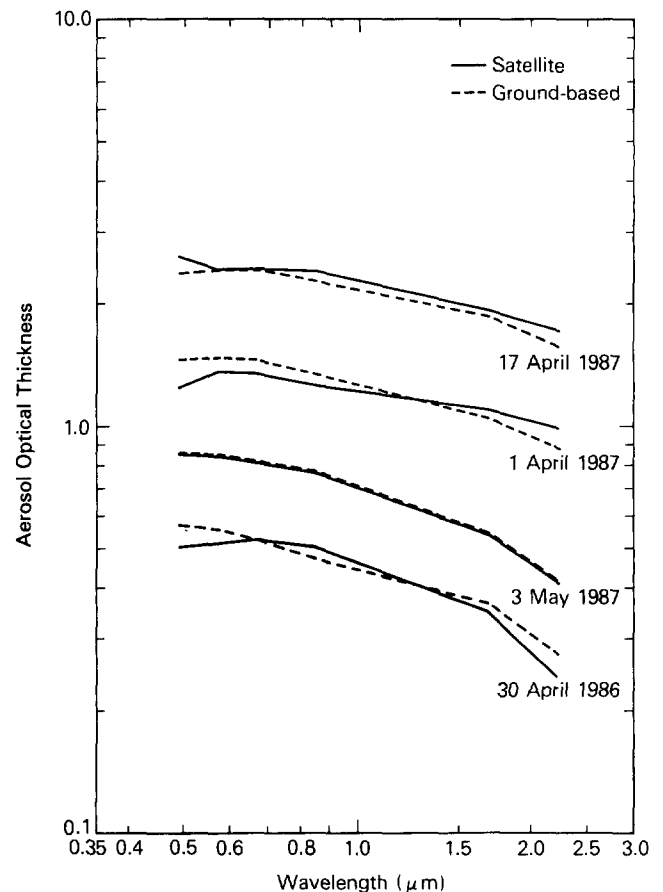


Fig. 18. Comparison between the spectral aerosol optical thickness derived from satellite images (solid curves) and ground-based measurements (dashed curves) over Senegal, Africa on 4 days during 1986 and 1987 [91].

conditions, however, $\tau_a(\lambda)$ can be derived with sufficiently high accuracy ($\Delta\tau_a \simeq 0.05$) to permit the spectral dependence of $\tau_a(\lambda)$ to be used to derive the columnar aerosol size distribution by numerical inversion methods. Furthermore, Spinhirne and King [87] have demonstrated the increased sensitivity to aerosol size distribution that results from having spectral optical thickness measurements available over a wide wavelength range, such as the $0.42 \leq \lambda \leq 2.13 \mu\text{m}$ range available from MODIS-N observations. As an example of the size distribution information contained in spectral aerosol optical thickness measurements, Fig. 20 illustrates measurements of the spectral aerosol optical thickness and estimated size distributions obtained from an airborne latitudinal survey beneath the El Chichón stratospheric aerosol layer [87]. The observed optical depths and corresponding standard deviations, obtained during May 1983 at latitudes of 45°N , 36°N and 17°N , are shown in the left-hand portion of the figure, while the size distributions and corresponding standard deviations obtained by inverting these data are shown in the right-hand portion. In lieu of $n_c(r)$ or, equivalently, dN_c/dr , our size distribution results are presented in terms of $dN_c/d\log r$, representing the number of particles per unit area per unit log radius interval in a vertical column through the atmosphere. The solid, dashed, and dot-dashed curves in the left portion of the figure indicate how the inverted size distributions

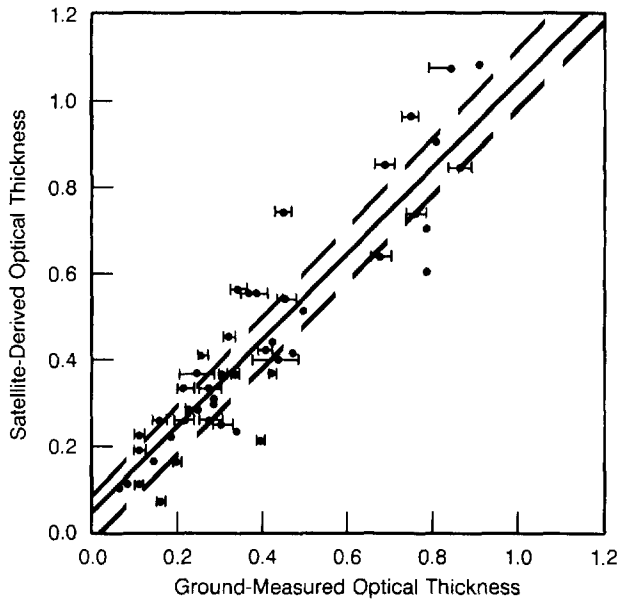


Fig. 19. Comparison of satellite and ground-based measurements of aerosol optical thickness obtained over the eastern U. S. during July and August 1980 and 1981. The continuous line is the best-fit regression line through all of the data, and the dashed lines include 68% of the possible regression lines using 1000 random subsets of the data. The ground-based measurements were obtained near Washington, Miami, and Columbus by J. Prospero (University of Miami), and the satellite-based measurements were derived from the GOES VISSR [27].

reproduce the $\tau_a(\lambda)$ measurements (i.e., the direct problem).

A number of different spectral optical thickness behaviors and corresponding aerosol size distributions can be found in [49], [46], [87]. These results clearly demonstrate that the slope and curvature (negative vs. positive) of the aerosol optical thickness as a function of wavelength is strongly correlated with the resulting size distribution. Over land, the aerosol optical thickness cannot be derived with sufficiently high accuracy to permit the derivation of the aerosol size distribution by direct inversion of $\tau_a(\lambda)$ measurements. Over dense dark vegetation we expect that the differences in the optical thickness between a clear and hazy day can be inferred to within an accuracy $\Delta\tau_a \approx 0.05$ in the blue and red channels. This will thus permit the derivation of perhaps one piece of information about the size distribution, such as its effective radius or the median size of a model log-normal distribution.

C. Dry Aerosol Mass Loading

Having determined the aerosol optical thickness and aerosol size distribution, it is rather straightforward to calculate the aerosol mass loading for a vertical column through the atmosphere, some fraction of which is composed of dry aerosol. Fraser *et al.* [27] developed an algorithm for estimating the columnar mass loading of particulate sulfur in a vertical column from satellite observations by noting further that the sulfate ion (SO_4^{2-}) is typically 30–60% of the total dry aerosol mass in the eastern U.S. [14]. In their algorithm, which did not benefit from any explicit knowledge of the shape of the aerosol size distribution, the total dry aerosol mass loading M (in units

of g m^{-2}) was estimated from an expression of the form

$$M = 0.18 f_d \omega_0 \tau_a (0.47 \mu\text{m}) \quad (12)$$

where ω_0 is the single scattering albedo of the aerosol particles and f_d the fraction of the total aerosol mass that is the dry aerosol component, itself a function of relative humidity h . Kaufman *et al.* [43] also showed that the coefficient appearing in the front of this expression is not greatly sensitive to the effective radius of the aerosol size distribution or its standard deviation for aerosols that are dominated by submicron sizes.

By assuming a mean value of $\omega_0 = 0.96$ and further taking into account the spectral dependence of the aerosol optical thickness between $0.61 \mu\text{m}$ (available from GOES satellite observations) and $0.47 \mu\text{m}$, Fraser *et al.* [27] were able to obtain a map of the columnar mass loading of particulate sulfur over the eastern U.S. on July 31, 1980. These results, illustrated in Fig. 21, show that the maximum concentration of sulfur aerosol can exceed 0.045 g m^{-2} , a value which occurred on this day over the Atlantic Ocean and West Virginia. For MODIS-N we intend to extend this procedure to continental and maritime regions by making further use of the spectral dependence of the aerosol optical thickness, together with estimates of the aerosol mean radius and dispersion in addition to estimates of the water vapor concentration in the boundary layer (see below).

D. Single Scattering Albedo

The aerosol single scattering albedo can be determined from satellite observations by examining the balance between aerosol scattering and absorption. This balance is demonstrated in Fig. 22, which shows the difference between the reflection function and surface reflectance as a function of surface reflectance for four values of the aerosol optical thickness ($\tau_a = 0.0, 0.2, 0.4$, and 0.6) and two values of the single scattering albedo ($\omega_0 = 0.81$ and 0.96). The reflection function $R(\tau_a, \omega_0; \mu, \mu_0, \phi)$ was computed for each case using (9) in a manner analogous to Fig. 11, where $\lambda = 0.61 \mu\text{m}$, $\theta_0 = 40^\circ$ and $\theta = 0^\circ$. For a dark surface ($A_g \ll 0.1$) the reflectance of the atmosphere (R_{atm}) dominates such that the reflection function is enhanced over that of the surface alone for both high and low aerosol absorption models. For a bright surface ($A_g \gg 0.3$), on the other hand, aerosol absorption as well as backscattering of the surface-reflected radiation dominate such that the reflection function of the earth-atmosphere system is reduced over that of the surface reflectance alone. For some intermediate critical surface reflectance A_g^c the radiative effect is zero, being nearly independent of the aerosol optical thickness. This critical surface reflectance A_g^c depends strongly on the single scattering albedo and, to a lesser extent, on particle size [25], [40]. As a direct consequence, the critical surface reflectance for which the reflection function does not change from a clear (low optical thickness) to hazy (high optical thickness) day can be used to determine the aerosol single scattering albedo.

Fig. 23 shows an example of an application of this method to Landsat-3MSS imagery of the Washington, DC area in the presence (hazy day) and absence (clear day) of forest

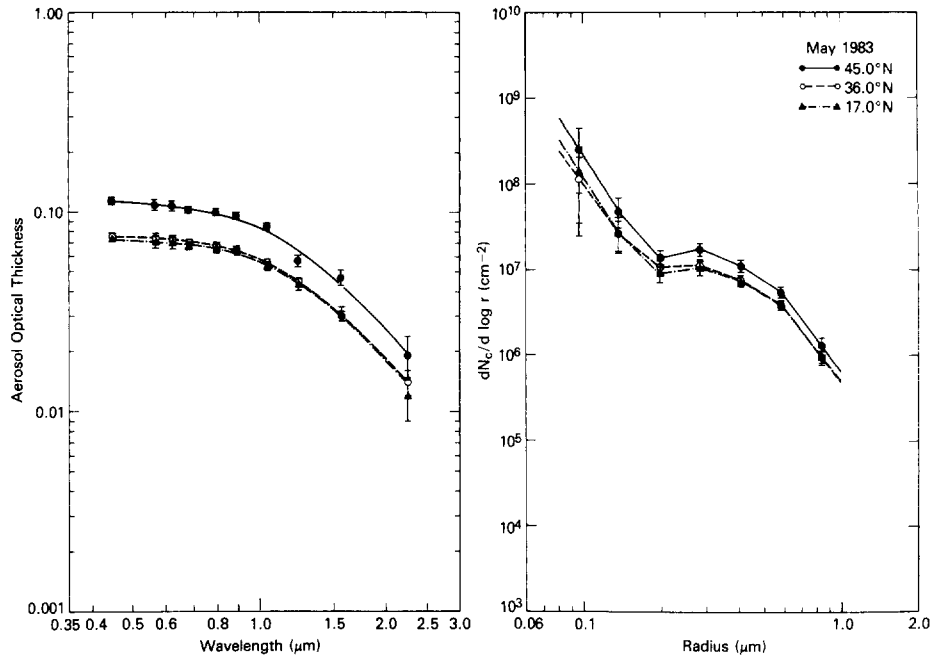


Fig. 20. Spectral aerosol optical thickness and estimated size distributions for the El Chichón stratospheric aerosol layer obtained from airborne measurements collected during May 1983 at latitudes of 45°N, 36°N, and 17°N. The smooth curves on the left indicate the regression fit to the data using the inverted size distributions. Standard deviations in the optical thickness measurements are shown on the left, with estimated standard deviations in the inverted size distributions shown on the right [87].

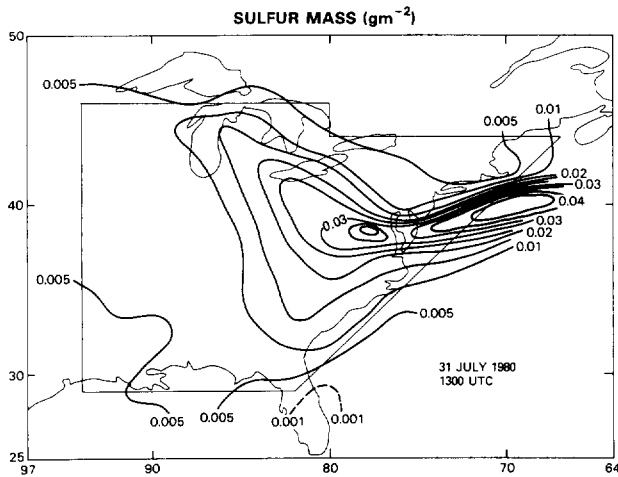


Fig. 21. Columnar mass loading of particulate sulfur obtained from GOES observations on July 31, 1980, in units of g m⁻² [27].

fire smoke. The arrow denotes the critical reflection function for which no change in brightness occurs as a result of the additional aerosol loading on the hazy day (August 2, 1982). From these observations Kaufman [40] inferred a single scattering albedo of 0.90 ± 0.01 with little dependence on wavelength, at least in the range $0.55 \leq \lambda \leq 0.75 \mu\text{m}$. This method for inferring the aerosol single scattering albedo is restricted to land regions in which there is a wide range of surface reflectances, necessarily including the critical value A_g^c .

If the surface is relatively uniform, the range of surface reflectance may be too small to enable the single scattering albedo to be derived using the method outlined above. Since

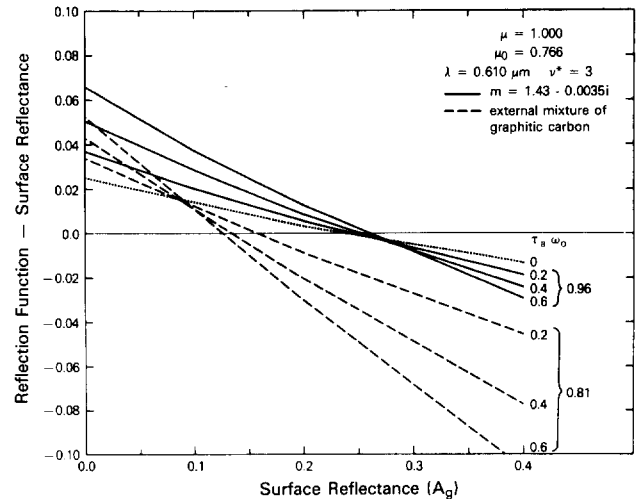


Fig. 22. Difference between the reflection function and surface reflectance at $0.61 \mu\text{m}$ as a function of surface reflectance for various values of the aerosol optical thickness τ_a and single scattering albedo ω_0 . The dotted line corresponds to results for a Rayleigh atmosphere and the solid and dashed lines to an aerosol-laden atmosphere having a Junge size distribution of the form $n(r) \propto r^{-4}$. Results apply to nadir observations ($\mu = 1$) when $\mu_0 = 0.766(\theta_0 = 40^\circ)$ [25].

the uniformity of the surface depends to a large extent on the spatial resolution of the sensor, an application of this method to 4 km AVHRR data limits this method largely to sea coast and lake shore regions [22], [43]. MODIS-N, on the other hand, will have 250-m channels that should exhibit high contrasts in surface reflectance over many land regions. In locales where spatial contrast is insufficient, spectral can be used to derive the single scattering albedo [43]. Vegetation is typically dark at $0.66 \mu\text{m}$ and yet quite bright at $0.87 \mu\text{m}$.

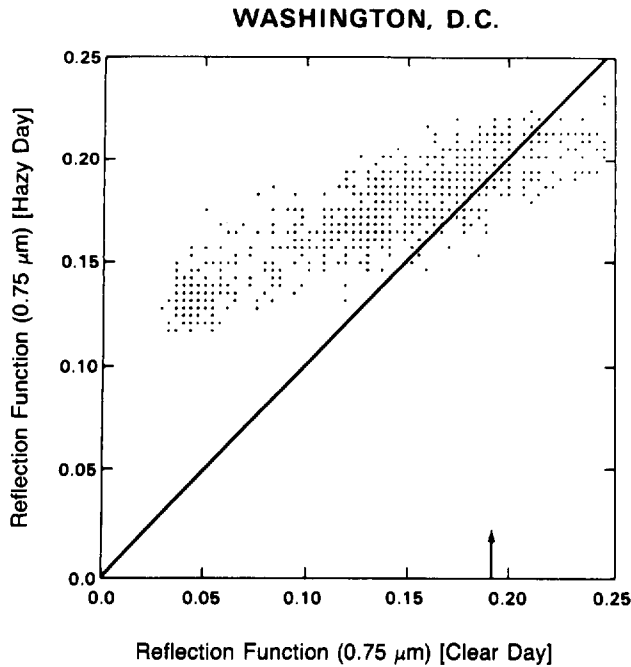


Fig. 23. Scatter diagram of the reflection functions of Landsat-3 MSS band 3 ($0.75 \mu\text{m}$) on a hazy day (August 2, 1982, $\theta_0 = 36^\circ$) as a function of the corresponding reflection function over Washington, DC obtained on a clear day (August 20, 1982, $\theta_0 = 33^\circ$). The arrow represents the value of the reflection function for which no change in brightness occurs as a result of the additional aerosol loading on the hazy day [25].

This characteristic, together with the assumption that the single scattering albedo is independent of wavelength in this spectral region, permits the single scattering albedo to be determined from the contrast in reflection function at these two channels for the same pixel. The single scattering albedo can thus be derived using a table lookup procedure in which the reflection function at both wavelengths is tabulated as a function of A_g , $\tau_a(\lambda)$, and ω_0 , where the relative optical thickness between the channels is governed by a predetermined aerosol size distribution model. An iterative procedure is adopted in which the optical thickness is determined from the difference in the reflection function at $0.66 \mu\text{m}$ between a clear and hazy day, and then applied to determine the single scattering albedo from the change in the reflection function in the near-infrared ($0.87 \mu\text{m}$). Both methods have recently been applied over a vegetated seashore in which good agreement between the methods was obtained [43].

E. Hybrid Methods

The aerosol optical thickness inferred from satellite observations depends on the assumed values of the particle size and single scattering albedo [27]. Similarly, the remote sensing of particle size or single scattering albedo depends on the other two aerosol properties assumed in the analysis. It is, therefore, advantageous to determine these three aerosol properties simultaneously using a self-consistent procedure. Kaufman *et al.* [43] developed such a hybrid method for determining the aerosol optical thickness, particle size, and single scattering albedo using AVHRR images obtained on 2 different days having substantially different aerosol loadings.

The method consists of an iterative procedure whereby a pair of images of a given region, obtained under similar viewing and solar illumination conditions and separated by a short time interval, are compared. In this way the effect of *a priori* assumptions on the aerosol optical and microphysical properties are greatly reduced. The two images correspond to a clear image containing background aerosol and a hazy image containing an aerosol episode of interest.

For satellite observations of a land–water interface in which the land consists of a vegetated surface with a small surface reflectance at $0.66 \mu\text{m}$ and a relatively large one at $0.87 \mu\text{m}$, the reflection function at each wavelength on the hazy and clear days, together with the surface reflectance of the water and land surfaces, yield eight measurements from which the aerosol optical thickness, particle size, and single scattering albedo can be determined using an iterative procedure. This method, described in detail by Kaufman *et al.* [43], first yields an estimate of the geometric mean mass radius of the aerosol particles, based primarily on the contrast in the reflection function between the clear and hazy days at $0.66 \mu\text{m}$, relative to that at $0.87 \mu\text{m}$, over the water surface. Having obtained an estimate of the particle size, the single scattering albedo is estimated from the contrast in the reflection function between the clear and hazy days over the water surface, relative to the land surface, at $0.87 \mu\text{m}$. Finally, the aerosol optical thickness is estimated for the hazy day from the reflection function at $0.66 \mu\text{m}$. This procedure is repeated until convergence is obtained (generally less than five iterations). Over land areas in the absence of a land–water interface, it is necessary to assume that the particle size is the same as over a nearby land–water interface. In this way the aerosol optical thickness and single scattering albedo can be derived simultaneously. Over water areas, on the other hand, the value of the single scattering albedo must be assumed to be the same as over a nearby land–water interface, thereby permitting the aerosol optical thickness and particle size to be derived simultaneously.

Figs. 24 and 25 show examples of the single scattering albedo and particle size obtained along a 5000-km trajectory of forest fire smoke transported from northeastern British Columbia to the east coast of the U.S. during late July and early August 1982 [22]. These aerosol properties, derived from an application of Kaufman *et al.*'s [43] method to NOAA-7 AVHRR satellite images, show that the size of the aerosol particles produced by the forest fire generally decreased with distance from the source, with a corresponding increase in the aerosol single scattering albedo.

Since the particle size and single scattering albedo derived using the above procedure depend primarily on the difference of the reflection function between a clear and hazy day, it necessarily follows that the aerosol optical thickness on the hazy day must exceed the aerosol optical thickness on the clear day by some critical value for a successful application of this approach, a value which Ferrare *et al.* [22] have estimated to be $\Delta\tau_a(0.66\mu\text{m}) \gtrsim 0.5$.

F. Implementation to MODIS-N

In our analysis of MODIS-N data, we plan to use the dark

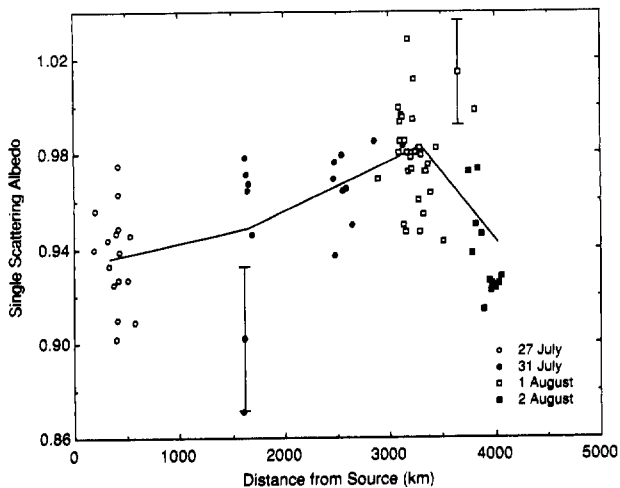


Fig. 24. Single scattering albedo of forest fire smoke as a function of distance from the source region in western Canada. The solid line represents the mean values of ω_0 computed for each day [22].

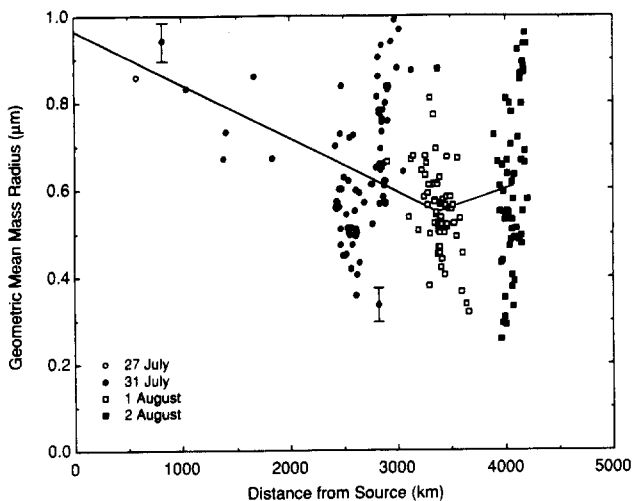


Fig. 25. As in Fig. 24 except for the geometric mean mass radius r_m (μm) [22].

vegetation method to routinely determine the aerosol optical thickness over land. Furthermore, we plan to determine the relative optical thickness in selected regions using a time sequence of images for which there are appropriate contrasts in surface reflectance. The method that will ultimately be selected will depend on the type of surface cover in the region, and will, consequently, vary with season and geographic location. Prior to the launch of EOS and the MODIS-N observatory, we plan to utilize existing satellite data as well as spectral and angular measurements to be obtained from the NASA ER-2 and University of Washington C-131A aircraft facilities. In order to validate the above specified methods, both for cloud and aerosol optical properties, we plan to conduct field experiments in which we coordinate Landsat TM overpasses with high-flying ER-2 overflights and *in situ* C-131A measurements. We are currently developing a 50-channel MODIS-N Airborne Simulator (MAS) for use on the ER-2 aircraft. This instrument will be a cross-track scanning spectrometer with many of the cloud and aerosol channels that

will be available on the satellite sensor. In addition, there are plans to install an international network of sunphotometers well in advance of the launch of EOS, a facility that will serve as a widely distributed ground-truth network for use in validating and improving the operational algorithms. Analysis of the mean particle size and aerosol size distribution will be performed routinely only in selected geographic regions. These data will routinely be validated against measurements from the network, primarily in locations where solar aureole measurements are also available. The single scattering albedo will be derived only in special cases using the hybrid method, and will make use of images having a significant difference in aerosol loading. We do not yet have contingency plans for validating this parameter on a global scale. During field experiments the single scattering albedo determined from an analysis of satellite or ER-2 observations can be compared with corresponding *in situ* measurements obtained aboard the C-131A.

VI. PRECIPITABLE WATER VAPOR

Present infrared sounders [90] are capable of retrieving water vapor profiles as a byproduct of the remote sensing of atmospheric temperature profiles. The derived water vapor profile depends in part on the initial guess for the temperature and moisture profile assumed in the inversion [35], being particularly sensitive to the assumed profiles close to the surface [74]. As far as we know, no systematic comparison of total precipitable water derived by inversion of HIRS/MSU data and radiosonde measurements has yet been published. Unpublished data (Susskind, private communication) suggest, however, that the absolute accuracy of the precipitable water derivation is approximately 20%. Recent radiosonde and sunphotometer measurements of total precipitable water over the Sahel [37] indicate virtually no correlation (r^2 between 0.01 and 0.28) with precipitable water derived from HIRS/MSU data [39]. Prabhakara *et al.* [62] developed an alternative approach for determining the total precipitable water over the oceans based on satellite microwave measurements, which they found to be capable of retrieving the total water vapor concentration with errors of the order of 10%. This method has not been applied over land due to the variability of the land emissivity at microwave frequencies.

In land regions where the difference between the surface and boundary layer temperatures is large, as in the Sahel region during the afternoon, Justice *et al.* [39] found a strong correlation between the infrared sensitivity to total precipitable water and sunphotometer measurements of water vapor. The infrared sensitivity to precipitable water used in this case was the difference in the brightness temperature between the 11 and 12 μm channels of AVHRR. In principle, if the apparent surface temperature, a function of the skin temperature and surface emissivity, is nearly equal to the average temperature of the boundary layer where most of the water vapor resides, infrared and microwave remote sensing will not be sensitive to boundary layer water vapor. In this case, any infrared or microwave photon emitted by the surface and absorbed by water vapor in the boundary layer will be reemitted at the

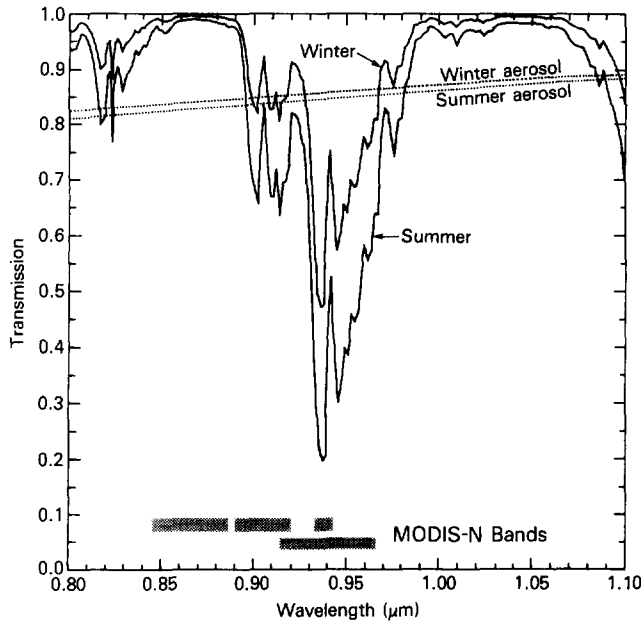


Fig. 26. Spectral transmission of the midlatitude summer and winter atmospheres in the presence of water vapor (solid lines) and aerosols (dashed lines). Computations were performed using LOWTRAN 7 for a slantpath through the atmosphere of 45° . The location and bandwidth of MODIS-N bands 2 and 17–19 are also shown in the figure [41].

temperature of the boundary layer, thereby having little effect on the upwelling brightness temperature. Therefore, though remote sensing of water vapor from AIRS/MHS is expected to yield accurate profiles of water vapor above the boundary layer, we anticipate that the transmission of solar radiation in the near-infrared will be more sensitive to water vapor in the boundary layer. As a consequence, the difference between the total precipitable water derived from the near-infrared channels on MODIS-N and the water vapor in the upper layers of the atmosphere derived from the infrared and microwave channels on AIRS/MHS will enable an accurate estimate of water vapor in the boundary layer to be inferred, especially over land.

For the remote sensing of the total column water vapor in cloud-free regions over land and in sunglint regions over water, MODIS-N will make use of selected water vapor absorption channels in the near-infrared. Fig. 26 illustrates the spectral transmission of the atmosphere in the $0.94 \mu\text{m}$ region of the near-infrared, based on LOWTRAN 7 [51] calculations for two model atmospheres, the midlatitude winter and midlatitude summer profiles. These calculations apply to the case of one-way transmission through the atmosphere when the solar zenith angle $\theta_0 = 45^\circ$. In this wavelength region three water vapor absorption channels have been selected as follows: (1) a wide channel at $0.940 \mu\text{m}$ for the purpose of retrieving the column water vapor content over land as well as from sunglint regions of the open oceans, (2) a narrower channel at $0.905 \mu\text{m}$ for determining large amounts of water vapor ($\geq 4 \text{ g cm}^{-2}$) or for retrieving water vapor under slant illumination and observation conditions, and (3) a narrow channel at $0.936 \mu\text{m}$ for retrieving small amounts of water vapor ($\lesssim 1 \text{ g cm}^{-2}$) and for retrieving water vapor above clouds.

The concept behind the derivation of the total precipitable

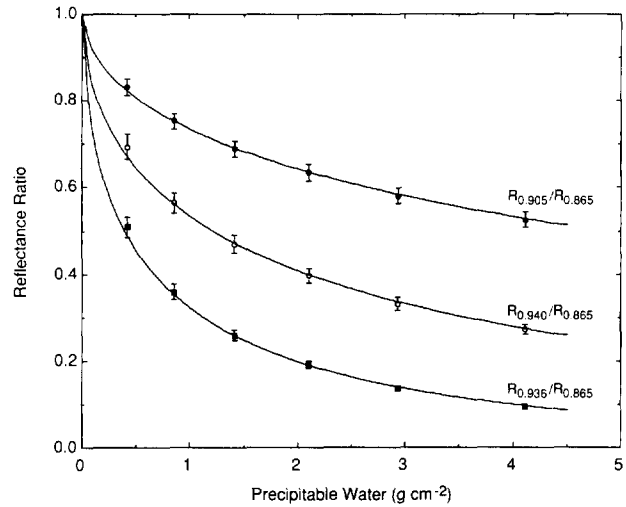


Fig. 27. The ratio of the reflection function at a weakly absorbing water vapor channel ($0.905 \mu\text{m}$), a moderately-absorbing water vapor channel ($0.940 \mu\text{m}$), and a strongly-absorbing water vapor channel ($0.936 \mu\text{m}$) to that in a nonabsorbing channel ($0.865 \mu\text{m}$) as a function of total precipitable water in a vertical column through the atmosphere. The error bars represent the variability in this function for 7 vegetation covers, 15 soil covers, and 2 snow covers [41]. The solid curves represent parameterization fits of the computations to equations of the form of (14). These calculations apply to the case of nadir observations ($\theta = 0^\circ$) when the solar zenith angle $\theta_0 = 40^\circ$.

water may be understood upon examination of Fig. 27, which shows the water vapor reflectance ratio

$$W(\lambda_{wv}) = \frac{R^{\lambda_{wv}}}{R^{0.865}} \quad (13)$$

as a function of total precipitable water for 7 vegetation covers, 15 soil covers, and 2 snow covers for the case of nadir observations ($\theta = 0^\circ$) when $\theta_0 = 40^\circ$. This function, first suggested by Gao and Goetz [28] and Kaufman and Gao [41], represents the ratio of the reflection function at a water vapor absorbing channel (λ_{wv}) to that at a neighboring nonabsorbing channel ($0.865 \mu\text{m}$ in the case of MODIS-N), and is seen to be a strong function of the total precipitable water and only weakly sensitive to uncertainties in the surface reflectance (represented here by error bars for 24 different surfaces). These results, based on simulations with LOWTRAN 7, show that the error in the directly derived water vapor amount is expected to be within $\pm 13\%$. If additional MODIS-N channels are used to reduce the uncertainty associated with the effects of haze, subpixel clouds, and temperature profile uncertainties, the error can be further reduced to $\pm 7\%$ [41].

Kaufman and Gao [41] have further shown that the water vapor reflectance ratio can be fit to a function of the form

$$W(\lambda_{wv}) = \alpha \exp(-\beta w^{1/2}) \quad (14)$$

where the coefficients α and β depend on the solar and observational zenith angles as well as the specific water vapor absorption channel (λ_{wv}) used in the analysis, and w is the total precipitable water in a vertical column through the atmosphere. The solid curves illustrated in Fig. 27 represent a fit of the numerical simulations to an equation of this form.

This method has been applied to Airborne Visible Infrared Imaging Spectrometer (AVIRIS) data obtained from the NASA

ER-2 aircraft over the Rogers Dry Lake of California and subsequently tested against radiosonde measurements. The total water vapor content derived from an application of this method was $2.6 \pm 0.2 \text{ g cm}^{-2}$, in contrast to $2.8 \pm 0.2 \text{ g cm}^{-2}$ derived from nearly coincident radiosonde ascents [41]. Further tests of this method were applied to AVIRIS data acquired over Denver, in which the two-channel method of Kaufman and Gao yielded a total water vapor content of $0.55 \pm 0.05 \text{ g cm}^{-2}$, in contrast to $0.67 \pm 0.2 \text{ g cm}^{-2}$ derived from nearly simultaneous ground-based microwave radiometer measurements.

VII. ATMOSPHERIC STABILITY

Atmospheric stability can best be determined from *in situ* measurements of the ambient and dew point temperature profiles. Infrared techniques to profile the atmosphere rely on cloud free measurements. While MODIS-N does not include all of the channels required for a full retrieval of the vertical distribution of temperature and water vapor, it does contain sufficient radiometric information to enable one to adjust the first guess temperature and moisture profiles to better reflect the local atmospheric state at the time of the satellite overpass. With its high spatial resolution, MODIS-N will further enable holes in cloudy scenes to be explored, thereby permitting the spatial structure of atmospheric stability to be determined on a global basis.

Through measurements in several narrow and carefully selected spectral intervals, the temperature of the atmosphere or the concentration of an attenuating gas, such as water vapor, can be inferred as a function of pressure by inverting the radiative transfer equation. Temperature profiles can be inferred from measurements in the CO_2 absorption bands near 4.3 and 15 μm , since CO_2 is a uniformly mixed gas, while water vapor profiles require additional measurements in the H_2O absorption band near 6.3 μm . Surface temperatures can also be inferred from observations in spectral regions where the atmosphere is the most transparent, such as 3.75, 8.55, 11.03, and 12.02 μm in the case of MODIS-N.

The computation of temperature and moisture profiles from a selected set of spectral intensity observations necessarily involves the following steps: (1) construction of first guess temperature and moisture profiles from a numerical forecast with analyzed surface data, (2) calculation of expected spectral intensities for the relevant spectral channels using a radiative transfer model, and (3) simultaneous solution in a least squares formulation of the radiative transfer equation in perturbation form to determine the adjustment in the guess temperature and moisture profiles necessary to better match the observed intensities [35]. Once the profiles of temperature and moisture have been determined, atmospheric stability can readily be computed.

One measure of the thermodynamic stability of the atmosphere is the total-totals index defined by [85]

$$TT = T^{850} + T_d^{850} - 2T^{500} \quad (15)$$

where T^{850} and T^{500} are the temperatures at the 850 and 500 mb levels, respectively, and T_d^{850} is the dewpoint temperature

at 850 mb. When warm moist air lies beneath a cold middle troposphere, as is common when tornados occur, TT typically lies between 50 and 60 K and intense convection can be expected. Using satellite observations, such as MODIS-N or AIRS, to derive the temperature and moisture profiles, it is more accurate to estimate layer mean values than precise values at specified levels. These, in turn, can be used to infer lapse rates, and thus it is more convenient to rewrite (15) as

$$TT = 2(T^{850} - T^{500}) - D^{850} \quad (16)$$

where $D^{850} = T^{850} - T_d^{850}$ is the dewpoint depression at 850 mb. Thus TT depends on the lapse rate of the lower atmosphere and the low level relative moisture concentration [85]. MODIS is ideally suited to the task of estimating global atmospheric total-totals stability.

VIII. SUMMARY AND CONCLUSIONS

In this paper we have outlined the basis for the majority of algorithms being developed for the purpose of inferring cloud, aerosol, and water vapor properties using MODIS-N and -T observations. The physical principles behind the determination of each of these parameters has been described, together with examples of their application to satellite and/or aircraft observations. These methods have all been developed and applied previously, but in the vast majority of instances have focused on case studies in selected geographical regions and under specific climatological conditions.

Table II summarizes the atmospheric parameters to be determined using MODIS-N observations, together with the principal channels to be used for their derivation. We have also listed the investigators responsible for producing the corresponding product as well as references to key papers containing further details of the methods. In addition to the parameters listed in this table and described herein, additional techniques are currently under development for determining the total ozone content using the ozone channel at 9.73 μm [52], precipitable water using the temperature and water vapor sounding channels (22–28) [35], and cloud top altitude using the water vapor channel at 0.936 μm [5].

The development of MODIS-N and -T represents an unprecedented opportunity in the earth sciences to increase our understanding of the earth–atmosphere–ocean system through spaceborne observations with multispectral radiometers capable of global surveys. In addition to the atmospheric processes to be explored using MODIS-N, the unique compliment of sensors offered by the MODIS observatory will permit terrestrial studies of tropical deforestation, areal extent, and distribution of acid rain on the boreal forests of Europe and North America, extent of desertification at the edge of the worlds deserts, and enhanced maps of the seasonal and interannual variation of global vegetation. Biological oceanographers will primarily utilize multispectral visible and near-infrared data to further explore the global distribution of phytoplankton biomass and ocean productivity begun with the Nimbus-7 Coastal Zone Color Scanner (CZCS). In addition, they will enhance our knowledge of the global sea surface temperature and its spatial and interannual variation. Perhaps of greatest significance

TABLE II
SUMMARY OF ATMOSPHERIC PARAMETERS AND PRINCIPAL CHANNELS USED FOR THEIR DERIVATION USING MODIS-N.

Parameter	Responsible Investigator	References	MODIS-N Channels
<i>Cloud properties</i>			
Optical thickness (τ_c)	King	[47], [58]	1, 7
Effective radius (r_e)	King, Menzel	[58], [4], [1]	1, 7, 20, 29, 31–32
Thermodynamic phase	King	[58], [20], [98]	1, 6, 7, 32
Cloud top pressure (p_c)	Menzel	[101], [54], [21]	32–36
Cloud top temperature (T_c)	Menzel	[89]	32–36
Effective emissivity (ϵ)	Menzel	[105], [63], [104]	31–32
Cloud fraction (f)	King	[80], [15], [98]	1, 6, 20, 29, 32
<i>Aerosol properties (land)</i>			
Optical thickness (τ_a)	Kaufman, Tanré	[42], [43], [91]	1–8
Effective radius (r_e)	Kaufman, Tanré	[42]	1–8
Single scattering albedo (ω_0)	Kaufman, Tanré	[25], [40], [43]	1–2
Mass loading (M)	Kaufman, Tanré	[27], [43], [22]	3
<i>Aerosol properties (water)</i>			
Optical thickness (τ_a)	Tanré, Kaufman	[8], [43]	1–8
Size distribution [$n_c(\tau)$]	Tanré, King	[49], [46], [87]	1–8
Mass loading (M)	Tanré, Kaufman	[27], [43], [22]	3
Precipitable water vapor (land)	Kaufman, Tanré	[41], [28]	2, 17–19
Precipitable water vapor (water)	Menzel	[35]	22–36
Atmospheric stability (TT)	Menzel	[85], [35]	22–36

is the unique opportunity for oceanographers, atmospheric scientists, and terrestrial ecosystem specialists to learn to work together and to further educate each other on the Earth as a global and integrated system.

ACKNOWLEDGMENT

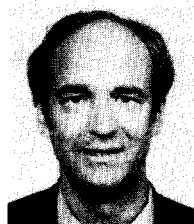
The authors are grateful to fellow MODIS team members V. V. Salomonson (Team Leader), W. E. Esaias (Oceans Group Leader), and C. O. Justice (Land Group Leader) for valuable discussions on the remote sensing of the earth-atmosphere system using MODIS-N. We are also grateful for useful comments on an earlier draft of this manuscript provided by B. A. Wielicki, R. S. Fraser, L. L. Stowe, and J. A. Coakley, Jr.

REFERENCES

- [1] S. A. Ackerman, W. L. Smith, J. D. Spinhirne, and H. E. Revercomb, "The 27–28 October 1986 FIRE IFO cirrus case study: Spectral properties of cirrus clouds in the 8–12 μm window," *Mon. Wea. Rev.*, vol. 118, pp. 2377–2388, 1990.
- [2] B. A. Albrecht, D. A. Randall, and S. Nicholls, "Observations of marine stratocumulus clouds during FIRE," *Bull. Amer. Meteorol. Soc.*, vol. 69, pp. 618–626, 1988.
- [3] P. A. Ardanuy, D. Han, and V. V. Salomonson, "The Moderate Resolution Imaging Spectrometer (MODIS) science and data system requirements," *IEEE Trans. Geosci. Remote Sensing*, vol. 29, pp. 75–88, 1991.
- [4] A. Arking and J. D. Childs, "Retrieval of cloud cover parameters from multispectral satellite images," *J. Climate Appl. Meteorol.*, vol. 24, pp. 322–333, 1985.
- [5] A. Arking, J. D. Childs, and J. Merritt, "Remote sensing of cloud cover parameters," in *Atmospheric Radiation: Progress and Prospects*, K. N. Liou and Z. Xiuji, Eds. Beijing: Science Press, PRC, 1987, pp. 473–488.
- [6] B. R. Barkstrom, "Earth radiation budget measurements: Pre-ERBE, ERBE, and CERES," in *Long-Term Monitoring of the Earth's Radiation Budget*, B. R. Barkstrom, Ed. (Proc. SPIE, vol. 1299), 1990, pp. 52–60.
- [7] L. W. Blank, "A new type of forest decline in Germany," *Nature*, vol. 314, pp. 311–314, 1985.
- [8] T. N. Carlson, "Atmospheric turbidity in Saharan dust outbreaks as determined by analyses of satellite brightness data," *Mon. Wea. Rev.*, vol. 107, pp. 322–335, 1979.
- [9] R. D. Cess, "Gauging water vapour feedback," *Nature*, vol. 342, pp. 736–737, 1989.
- [10] R. D. Cess, G. L. Potter, J. P. Blanchet, G. J. Boer, S. J. Ghan, J. T. Kiehl, H. Le Treut, Z. X. Li, X. Z. Liang, J. F. B. Mitchell, J. J. Morcrette, D. A. Randall, M. R. Riches, E. Roeckner, U. Schlese, A. Slingo, K. E. Taylor, W. M. Washington, R. T. Wetherald, and I. Yagai, "Interpretation of cloud-climate feedback as produced by 14 atmospheric general circulation models," *Science*, vol. 245, pp. 513–516, 1989.
- [11] M. T. Chahine, "Remote sounding of cloudy atmospheres. I. The single cloud layer," *J. Atmos. Sci.*, vol. 31, pp. 233–243, 1975.
- [12] S. Chandrasekhar, *Radiative Transfer*. New York: Dover, 1960, p. 273.
- [13] R. J. Charlson, J. E. Lovelock, M. O. Andreae, and S. G. Warren, "Oceanic phytoplankton, atmospheric sulphur, cloud albedo and climate," *Nature*, vol. 326, pp. 655–661, 1987.
- [14] R. J. Charlson, A. H. Vanderpol, D. S. Covert, A. P. Waggoner, and N. C. Ahlquist, "Sulfuric acid-ammonium sulfate aerosol: Optical detection in the St. Louis region," *Science*, vol. 184, pp. 156–158, 1974.
- [15] J. A. Coakley, Jr. and F. P. Bretherton, "Cloud cover from high-resolution scanner data: Detecting and allowing for partially filled fields of view," *J. Geophys. Res.*, vol. 87, pp. 4917–4932, 1982.
- [16] J. A. Coakley, Jr., R. L. Bernstein, and P. A. Durkee, "Effect of ship-track effluents on cloud reflectivity," *Science*, vol. 237, pp. 1020–1022, 1987.
- [17] R. J. Curran and M. L. C. Wu, "Skylab near-infrared observations of clouds indicating supercooled liquid water droplets," *J. Atmos. Sci.*, vol. 39, pp. 635–647, 1982.
- [18] R. J. Curran, H. L. Kyle, L. R. Blaine, J. Smith, and T. D. Clem,

- "Multichannel scanning radiometer for remote sensing cloud physical parameters," *Rev. Sci. Instrum.*, vol. 52, pp. 1546–1555, 1981.
- [19] E. Ebert, "A pattern recognition technique for distinguishing surface and cloud types in the polar regions," *J. Climate Appl. Meteorol.*, vol. 26, pp. 1412–1427, 1987.
 - [20] E. E. Ebert, "Analysis of polar clouds from satellite imagery using pattern recognition and a statistical cloud analysis scheme," *J. Appl. Meteorol.*, vol. 28, pp. 382–399, 1989.
 - [21] J. R. Eyre, and W. P. Menzel, "Retrieval of cloud parameters from satellite sounder data: A simulation study," *J. Appl. Meteorol.*, vol. 28, pp. 267–275, 1989.
 - [22] R. A. Ferrare, R. S. Fraser, and Y. J. Kaufman, "Satellite measurements of large scale air pollution: Measurements of forest fire smoke," *J. Geophys. Res.*, vol. 92, pp. 9911–9925, 1990.
 - [23] J. S. Foot, "Some observations of the optical properties of clouds. I: Stratocumulus," *Quart. J. Roy. Meteorol. Soc.*, vol. 114, pp. 129–144, 1988.
 - [24] R. S. Fraser, "Satellite measurement of mass of Sahara dust in the atmosphere," *Appl. Opt.*, vol. 15, pp. 2471–2479, 1976.
 - [25] R. S. Fraser and Y. J. Kaufman, "The relative importance of aerosol scattering and absorption in remote sensing," *IEEE Trans. Geosci. Remote Sensing*, vol. 23, pp. 625–633, 1985.
 - [26] R. S. Fraser, O. P. Bahethi, and A. H. Al-Abbas, "The effect of the atmosphere on the classification of satellite observations to identify surface features," *Remote Sensing Environ.*, vol. 6, pp. 229–249, 1977.
 - [27] R. S. Fraser, Y. J. Kaufman, and R. L. Mahoney, "Satellite measurements of aerosol mass and transport," *Atmos. Environ.*, vol. 18, pp. 2577–2584, 1984.
 - [28] B. C. Gao and A. F. H. Goetz, "Column atmospheric water vapor retrievals from airborne imaging spectrometer data," *J. Geophys. Res.*, vol. 95, pp. 3549–3564, 1990.
 - [29] B. C. Gao and A. F. H. Goetz, "Cloud area determination from AVIRIS data using water vapor channels near 1 μm ," *J. Geophys. Res.*, vol. 96, pp. 2857–2864, 1991.
 - [30] M. Griggs, "Measurements of atmospheric aerosol optical thickness over water using ERTS-1 data," *J. Air Pollut. Contr. Ass.*, vol. 25, pp. 622–626, 1975.
 - [31] G. G. Gutman, "Satellite daytime image classification for global studies of earth's surface parameters from polar orbiters," *Int. J. Remote Sensing*, in press, 1991.
 - [32] J. E. Hansen and A. A. Lacis, "Sun and dust versus greenhouse gases: An assessment of their relative roles in global climate change," *Nature*, vol. 346, pp. 713–719, 1990.
 - [33] J. E. Hansen and J. B. Pollack, "Near-infrared light scattering by terrestrial clouds," *J. Atmos. Sci.*, vol. 27, pp. 265–281, 1970.
 - [34] J. E. Hansen and L. D. Travis, "Light scattering in planetary atmospheres," *Space Sci. Rev.*, vol. 16, pp. 527–610, 1974.
 - [35] C. M. Hayden, "GOES-VAS simultaneous temperature moisture retrieval algorithm," *J. Appl. Meteorol.*, vol. 27, pp. 705–733, 1988.
 - [36] G. M. Hidy, P. K. Mueller, and E. Y. Tong, "Spatial and temporal distribution of airborne sulfate in parts of the United States," *Atmos. Environ.*, vol. 12, pp. 735–752, 1978.
 - [37] B. N. Holben, T. F. Eck, and R. S. Fraser, "Temporal and spatial variability of aerosol optical depth in the Sahel region in relation to vegetation remote sensing," *Int. J. Remote Sensing*, vol. 12, pp. 1147–1163, 1991.
 - [38] J. G. Hudson, "Effects of CCN concentrations on stratus clouds," *J. Atmos. Sci.*, vol. 40, pp. 480–486, 1983.
 - [39] C. O. Justice, T. F. Eck, D. Tanré, and B. N. Holben, "The effect of water vapor on the Normalized Difference Vegetation Index derived for the Sahelian region from NOAA AVHRR data," *Int. J. Remote Sensing*, vol. 12, pp. 1165–1187, 1991.
 - [40] Y. J. Kaufman, "Satellite sensing of aerosol absorption," *J. Geophys. Res.*, vol. 92, pp. 4307–4317, 1987.
 - [41] Y. J. Kaufman and B. C. Gao, "Remote sensing of water vapor in the near IR from EOS/MODIS," *IEEE Trans. Geosci. Remote Sensing*, in press, 1991.
 - [42] Y. J. Kaufman and C. Sendra, "Algorithm for automatic atmospheric corrections to visible and near-IR satellite imagery," *Int. J. Remote Sensing*, vol. 9, pp. 1357–1381, 1988.
 - [43] Y. J. Kaufman, R. S. Fraser, and R. A. Ferrare, "Satellite measurements of large-scale air pollution: Method," *J. Geophys. Res.*, vol. 95, pp. 9895–9909, 1990.
 - [44] Y. J. Kaufman, R. S. Fraser, and R. L. Mahoney, "Fossil fuel and biomass burning effect on climate—heating or cooling?" *J. Climate*, vol. 4, pp. 578–588, 1991.
 - [45] Y. J. Kaufman, C. J. Tucker, and I. Fung, "Remote sensing of biomass burning in the tropics," *J. Geophys. Res.*, vol. 95, pp. 9926–9939, 1990.
 - [46] M. D. King, "Sensitivity of constrained linear inversions to the selection of the Lagrange multiplier," *J. Atmos. Sci.*, vol. 39, pp. 1356–1369, 1982.
 - [47] M. D. King, "Determination of the scaled optical thickness of clouds from reflected solar radiation measurements," *J. Atmos. Sci.*, vol. 44, pp. 1734–1751, 1987.
 - [48] M. D. King, L. F. Radke, and P. V. Hobbs, "Determination of the spectral absorption of solar radiation by marine stratocumulus clouds from airborne measurements within clouds," *J. Atmos. Sci.*, vol. 47, pp. 894–907, 1990.
 - [49] M. D. King, D. M. Byrne, B. M. Herman, and J. A. Reagan, "Aerosol size distributions obtained by inversion of spectral optical depth measurements," *J. Atmos. Sci.*, vol. 35, pp. 2153–2167, 1978.
 - [50] M. D. King, M. G. Strange, P. Leone, and L. R. Blaine, "Multi-wavelength scanning radiometer for airborne measurements of scattered radiation within clouds," *J. Atmos. Oceanic Tech.*, vol. 3, pp. 513–522, 1986.
 - [51] F. X. Kneizys, E. P. Shettle, L. W. Abreu, J. H. Chetwynd, G. P. Anderson, W. O. Gallery, J. E. A. Selby, and S. A. Clough, "Users guide to LOWTRAN 7," AFGL-TR-88-0177, Air Force Geophysics Laboratories, Hanscom AFB, 137 pp., 1988.
 - [52] X. L. Ma, W. L. Smith, and H. M. Woolf, "Total ozone from NOAA satellites—a physical model for obtaining measurements with high spatial resolution," *J. Climate Appl. Meteorol.*, vol. 23, pp. 1309–1314, 1984.
 - [53] D. J. McCleese and L. S. Wilson, "Cloud top heights from temperature sounding instruments," *Quart. J. Roy. Meteorol. Soc.*, vol. 102, pp. 781–790, 1983.
 - [54] W. P. Menzel, W. L. Smith, and T. R. Stewart, "Improved cloud motion wind vector and altitude assignment using VAS," *J. Climate Appl. Meteorol.*, vol. 22, pp. 377–384, 1983.
 - [55] W. P. Menzel, D. P. Wylie, and K. I. Strabala, "Seasonal and diurnal changes in cirrus clouds as seen in four years of observations with the VAS," *J. Appl. Meteorol.*, in press, 1991.
 - [56] P. Minnis and E. F. Harrison, "Diurnal variability of regional cloud and clear-sky radiative parameters derived from GOES data. Part I: Analysis method," *J. Climate Appl. Meteorol.*, vol. 23, pp. 993–1011, 1984.
 - [57] J. F. B. Mitchell, C. A. Senior, and W. J. Ingram, "CO₂ and climate: A missing feedback?," *Nature*, vol. 341, pp. 132–134, 1989.
 - [58] T. Nakajima and M. D. King, "Determination of the optical thickness and effective particle radius of clouds from reflected solar radiation measurements. Part I: Theory," *J. Atmos. Sci.*, vol. 47, pp. 1878–1893, 1990.
 - [59] T. Nakajima, M. D. King, J. D. Spinhirne, and L. F. Radke, "Determination of the optical thickness and effective particle radius of clouds from reflected solar radiation measurements. Part II: Marine stratocumulus observations," *J. Atmos. Sci.*, vol. 48, pp. 728–750, 1991.
 - [60] P. Pilewskie and S. Twomey, "Discrimination of ice from water in clouds by optical remote sensing," *Atmos. Res.*, vol. 21, pp. 113–122, 1987.
 - [61] P. Pilewskie and S. Twomey, "Cloud phase discrimination by reflectance measurements near 1.6 and 2.2 μm ," *J. Atmos. Sci.*, vol. 44, pp. 3419–3420, 1987.
 - [62] C. Prabhakara, H. D. Chang, and A. T. C. Chang, "Remote sensing of precipitable water over the oceans from Nimbus 7 microwave measurements," *J. Appl. Meteorol.*, vol. 31, pp. 59–68, 1982.
 - [63] C. Prabhakara, R. S. Fraser, G. Dalu, M. L. C. Wu, and R. J. Curran, "Thin cirrus clouds: Seasonal distribution over oceans deduced from Nimbus-4 IRIS," *J. Appl. Meteorol.*, vol. 27, pp. 379–399, 1988.
 - [64] C. Prabhakara, J. M. Yoo, G. Dalu, and R. S. Fraser, "Deep optically thin cirrus clouds in the polar regions. Part I: Infrared extinction characteristics," *J. Appl. Meteorol.*, vol. 29, pp. 1313–1329, 1990.
 - [65] J. M. Prospero, "Arid regions as source of mineral aerosols in the marine atmosphere," *Geolog. Soc. Amer.*, Spec. pap. 186, pp. 71–86, 1981.
 - [66] L. F. Radke, J. A. Coakley, Jr., and M. D. King, "Direct and remote sensing observations of the effects of ships on clouds," *Science*, vol. 246, pp. 1146–1149, 1989.
 - [67] L. F. Radke, J. L. Stith, D. A. Hegg, and P. V. Hobbs, "Airborne studies of particles and gases from forest fires," *J. Air Pollut. Contr. Ass.*, vol. 28, pp. 30–34, 1978.
 - [68] V. Ramanathan, "The role of earth radiation budget studies in climate and general circulation research," *J. Geophys. Res.*, vol. 92, pp. 4075–4095, 1987.
 - [69] V. Ramanathan, B. R. Barkstrom, and E. F. Harrison, "Climate and the earth's radiation budget," *Phys. Today*, vol. 42, pp. 22–32, 1989.
 - [70] V. Ramanathan, R. D. Cess, E. F. Harrison, P. Minnis, B. R. Barkstrom, E. Ahmad, and D. Hartmann, "Cloud-radiative forcing and climate: Results from the Earth Radiation Budget Experiment," *Science*, vol. 243, pp. 57–63, 1989.
 - [71] C. R. N. Rao, L. L. Stowe, and L. L. McClain, "Remote sensing

- of aerosol over the oceans using AVHRR data: Theory, practice, and applications," *Int. J. Remote Sensing*, vol. 10, pp. 743-749, 1989.
- [72] A. Raval and V. Ramanathan, "Observational determination of the greenhouse effect," *Nature*, vol. 342, pp. 758-761, 1989.
 - [73] F. Rawlins and J. S. Foot, "Remotely sensed measurements of stratocumulus properties during FIRE using the C130 aircraft multichannel radiometer," *J. Atmos. Sci.*, vol. 47, 2488-2503, 1990.
 - [74] D. Reuter, J. Susskind, and A. Pursch, "First-guess dependence of a physically based set of temperature-humidity retrievals from HIRS2/MSU data," *J. Atmos. Oceanic Technol.*, vol. 5, pp. 70-83, 1988.
 - [75] E. Roeckner, U. Schlese, J. Biercamp, and P. Loewe, "Cloud optical depth feedbacks and climate modeling," *Nature*, vol. 329, pp. 138-140, 1987.
 - [76] W. B. Rossow and R. A. Schiffer, "ISCCP cloud data products," *Bull. Amer. Meteorol. Soc.*, vol. 72, pp. 2-20, 1991.
 - [77] W. B. Rossow, L. C. Gardner, and A. A. Lacis, "Global seasonal cloud variations from satellite radiance measurements. Part I: Sensitivity of analysis," *J. Climate*, vol. 2, pp. 419-458, 1989.
 - [78] W. B. Rossow, F. Mosher, E. Kinsella, A. Arking, M. Despois, E. Harrison, P. Minnis, E. Ruprecht, G. Seze, C. Simmer, and E. Smith, "ISCCP cloud algorithm intercomparison," *J. Appl. Meteorol.*, vol. 24, pp. 877-903, 1985.
 - [79] R. W. Saunders, "An automated scheme for the removal of cloud contamination from AVHRR radiances over western Europe," *Int. J. Remote Sensing*, vol. 7, pp. 867-886, 1986.
 - [80] R. W. Saunders and K. T. Kriebel, "An improved method for detecting clear sky and cloudy radiances from AVHRR data," *Int. J. Remote Sensing*, vol. 9, pp. 123-150, 1988.
 - [81] L. Schütz, "Long range transport of desert dust with special emphasis on the Sahara," *Ann. N.Y. Acad. Sci.*, vol. 338, pp. 515-532, 1980.
 - [82] A. Slingo, "A GCM parameterization for the shortwave radiative properties of water clouds," *J. Atmos. Sci.*, vol. 46, pp. 1419-1427, 1989.
 - [83] W. L. Smith and R. Frey, "On cloud altitude determinations from High Resolution Interferometer Sounder (HIS) observations," *J. Appl. Meteorol.*, vol. 29, pp. 658-662, 1990.
 - [84] W. L. Smith and C. M. R. Platt, "Intercomparison of radiosonde, ground based laser and satellite deduced cloud heights," *J. Appl. Meteorol.*, vol. 17, pp. 1796-1802, 1978.
 - [85] W. L. Smith and F. X. Zhou, "Rapid extraction of layer relative humidity, geopotential thickness, and atmospheric stability from satellite sounding radiometer data," *Appl. Opt.*, vol. 21, pp. 924-928, 1982.
 - [86] J. D. Spinhirne and W. D. Hart, "Cirrus structure and radiative parameters from airborne lidar and spectral radiometer observations," *Mon. Wea. Rev.*, vol. 118, 2329-2343, 1990.
 - [87] J. D. Spinhirne and M. D. King, "Latitudinal variation of spectral optical thickness and columnar size distribution of the El Chichon stratospheric aerosol layer," *J. Geophys. Res.*, vol. 90, pp. 10 607-10 619, 1985.
 - [88] L. L. Stowe, E. P. McClain, R. Carey, P. Pellegrino, G. Gutman, P. Davis, C. Long, and S. Hart, "Global distribution of cloud cover derived from NOAA/AVHRR operational satellite data," *Adv. Space Res.*, vol. 11, pp. 51-54, 1991.
 - [89] J. Susskind, D. Reuter, and M. T. Chahine, "Cloud fields retrieved from analysis of HIRS2/MSU sounding data," *J. Geophys. Res.*, vol. 92, pp. 4035-4050, 1987.
 - [90] J. Susskind, J. Rosenfield, D. Reuter, and M. T. Chahine, "Remote sensing of weather and climate parameters from HIRS2/MSU on TIROS-N," *J. Geophys. Res.*, vol. 88, pp. 4677-4699, 1984.
 - [91] D. Tanré, P. Y. Deschamps, C. Devaux, and M. Herman, "Estimation of Saharan aerosol optical thickness from blurring effects in Thematic Mapper data," *J. Geophys. Res.*, vol. 93, pp. 15 955-15 964, 1988.
 - [92] S. Twomey, "Cloud nucleation in the atmosphere and the influence of nucleus concentration levels in atmospheric physics," *J. Phys. Chem.*, vol. 84, pp. 1459-1463, 1980.
 - [93] S. Twomey and T. Cocks, "Remote sensing of cloud parameters from spectral reflectance in the near-infrared," *Beitr. Phys. Atmos.*, vol. 62, pp. 172-179, 1989.
 - [94] S. Twomey, M. Piepgrass, and T. L. Wolfe, "An assessment of the impact of pollution on global cloud albedo," *Tellus*, vol. 36, pp. 356-366, 1984.
 - [95] H. C. van de Hulst, *Multiple Light Scattering, Tables, Formulas, and Applications*, vol. 1. New York: Academic Press, 1980, pp. 76-82.
 - [96] D. E. Ward, "Field scale measurements of emission from open fires," in *Proc. Defense Nuclear Agency Global Effects Review*, Defense Nuclear Agency (Washington, DC), 1986.
 - [97] R. M. Welch, M. S. Navar, and S. K. Sengupta, "The effect of spatial resolution upon texture-based cloud field classification," *J. Geophys. Res.*, vol. 94, pp. 14 781-14 781, 1989.
 - [98] R. M. Welch, S. K. Sengupta, and K. S. Kuo, "Marine stratocumulus cloud fields off the coast of southern California observed using LANDSAT imagery. Part II: Textural analysis," *J. Appl. Meteorol.*, vol. 27, pp. 363-378, 1988.
 - [99] R. T. Wetherald and S. Manabe, "Cloud feedback processes in a general circulation model," *J. Atmos. Sci.*, vol. 45, pp. 1397-1415, 1988.
 - [100] K. T. Whitby, "The physical characteristics of sulfur aerosols," *Atmos. Environ.*, vol. 12, pp. 135-159, 1978.
 - [101] B. A. Wielicki and J. A. Coakley, Jr., "Cloud retrieval using infrared sounder data: Error analysis," *J. Appl. Meteorol.*, vol. 20, pp. 157-169, 1981.
 - [102] B. A. Wielicki and L. Parker, "On the determination of cloud cover from satellite sensors: The effect of sensor spatial resolution," Submitted to *J. Geophys. Res.*, 1991.
 - [103] T. M. L. Wigley, "Possible climate change due to SO₂-derived cloud condensation nuclei," *Nature*, vol. 339, pp. 355-357, 1989.
 - [104] M. L. C. Wu, "A method for remote sensing the emissivity, fractional cloud cover and cloud top temperature of high-level, thin clouds," *J. Appl. Meteorol.*, vol. 26, pp. 225-233, 1987.
 - [105] D. P. Wylie and W. P. Menzel, "Two years of cloud cover statistics using VAS," *J. Climate*, vol. 2, pp. 380-392, 1989.



Michael D. King received the B.A. degree in physics from Colorado College in 1971, and the M.S. and Ph.D. degrees in atmospheric sciences from the University of Arizona in 1973 and 1977, respectively.

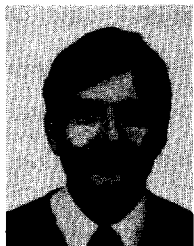
He is a senior atmospheric scientist in the Laboratory for Atmospheres at NASA Goddard Space Flight Center, where he has been a research scientist since 1978. He is a member of the MODIS and CERES Science Teams of EOS, and has been the leader of the atmosphere discipline group of MODIS since 1989. In addition to these positions, he was a visiting professor at the University of Washington from 1986 to 1987 and has been Project Scientist of the Earth Radiation Budget Experiment (ERBE), since 1983, and a member of the ERBE Science Team, since 1980, and the First ISCCP Regional Experiment (FIRE) Science Experiment Team, since 1985. His research experience includes conceiving, developing, and operating multispectral scanning radiometers from a number of aircraft platforms in field experiments ranging from arctic stratus clouds off Barrow, AK, to smoke from the Kuwait oil fires in the Persian Gulf. He is currently leading an effort to develop a MODIS-N Airborne Simulator for the NASA ER-2 aircraft to aid in the development of atmospheric and land remote sensing algorithms for MODIS-N prior to the launch of EOS-A1.

Dr. King is a fellow of the American Meteorological Society, where he served as Chairman of the Committee on Atmospheric Radiation from 1986 to 1988 and Chairman of the 6th Conference on Atmospheric Radiation in 1986, and has been Associate Editor of the *Journal of the Atmospheric Sciences* since 1991. He was awarded the NASA Exceptional Service Medal in 1985 and the Goddard Space Flight Center Special Achievement Award in 1983.



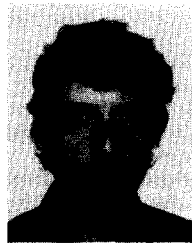
Yoram J. Kaufman received the B.Sc. and M.Sc. degrees in physics from the Technion-Israel Institute of Technology, Israel, in 1972 and 1974, respectively, and the Ph.D. degree from Tel-Aviv University in 1979. He came to NASA Goddard Space Flight Center in 1979 as an NRC Resident Research Associate. He is currently an atmospheric scientist in the Laboratory for Atmospheres at NASA Goddard Space Flight Center.

His present research includes theoretical and experimental investigations in atmospheric science, radiative transfer, and remote sensing. His research experience includes remote sensing of aerosols and clouds, atmospheric correction of satellite imagery of the earth's surface, interaction of aerosols with clouds and their subsequent impact on climate, remote sensing of emissions from biomass burning in the tropics, and calibration of satellite sensors. He has conducted field experiments that include airborne and ground-based measurements of aerosol properties (smoke aerosol, dust, and anthropogenic aerosol) and their effect on radiative transfer. He has been a member of the MODIS Science Team since 1989. Three of his papers on properties of CO₂ lasers and saturable absorbers, based on research conducted while at the Technion Institute, were selected for the SPIE Milestone Series "of outstanding papers from the world literature on optical and optoelectronic science: Selected Papers on CO₂ Lasers."



W. Paul Menzel was born in Heidenheim, Germany in 1945. He received the B.S. degree in physics from the University of Maryland, College Park, MD, in 1967, and the M.S. and Ph.D. degrees in theoretical solid state physics from the University of Wisconsin in 1968 and 1974, respectively.

His early work focused on calculating the band structure properties of alkali halides using the method of linear combinations of atomic orbitals in a Hartree-Fock formation. In 1975 he joined the Space Science and Engineering Center at the University of Wisconsin, where he was among the first to explore the possibilities for remote sensing of the earth's atmosphere from a geosynchronous satellite. Specifications for the vertical temperature and moisture sounding capabilities of the Visible and Infrared Spin Scan Radiometer (VISSR) Atmospheric Sounder (VAS) were the result of that work. In 1983 he joined NOAA/NESDIS to head the Advanced Satellite Products Project, where he is responsible for the development, testing, and evaluation of procedures for deriving new atmospheric products from spaceborne observations. This activity focuses on transferring advances made in the research laboratory to the operational weather forecaster. Since 1989, he has been a member of the MODIS Science Team, through which he is developing and flying passive infrared radiometers on the NASA ER-2 aircraft for the purpose of investigating cloud properties from multispectral data of high spatial resolution. Dr. Menzel is an adjunct professor of Meteorology at the University of Wisconsin and co-Chairman of the International TIROS Operational Vertical Sounder (TOVS) Working Group.



Didier D. Tanré received the M.Sc. degree in physics in 1975 and the "Thèse de 3ème Cycle" and "Doctorat d'Etat" in atmospheric physics in 1977 and 1982, respectively, all from the Université des Sciences et Techniques de Lille, France. He is an atmospheric scientist in the CNRS (Centre National de la Recherche Scientifique), collocated with the Laboratoire d'Optique Atmosphérique at the Université des Sciences et Techniques de Lille, Villeneuve d'Ascq, France, where he has been a research scientist since 1982. He has been a member

of the MODIS Science Teams since 1989. In addition to these positions he was an NRC Resident Research Associate at NASA Goddard Space Flight Center from 1989 through 1991. His research experience includes radiative transfer modeling through realistic atmospheres, both theory and applications. His interests also include remote sensing of atmospheric properties from satellite and ground-based observations as well as atmospheric effects in satellite imagery of the earth's surface.